ROYAL SOCIETY
OF CHEMISTRY

PAPER

Check for updates

Disorder in $Ho_2Ti_{2-x}Zr_xO_7$: pyrochlore to defect fluorite solid solution series

Devon L. Drey, [iD] [a] Eric C. O'Quinn,[a] Tamilarasan Subramani,[b] Kristina Lilova,[b] Gianguido Baldinozzi,[c] Igor M. Gussev,[a] Antonio F. Fuentes, [iD] [d] Joerg C. Neuefeind,[e] Michelle Everett,[e] David Sprouster, [iD] [f] Alexandra Navrotsky,[b] Rodney C. Ewing[g] and Maik Lang*[a]

Pyrochlore ($A_2B_2O_7$) is an important, isometric structure-type because of its large variety of compositions and structural derivatives that are generally related to different disordering mechanisms at various spatial scales. The disordering is key to understanding variations in properties, such as magnetic behavior or ionic conduction. Neutron and X-ray total scattering methods were used to investigate the degree of structural disorder in the $Ho_2Ti_{2-x}Zr_xO_7$ ($x = 0.0-2.0$, $\Delta x = 0.25$) solid solution series as a function of the Zr-content, x. Ordered pyrochlores ($Fd\bar{3}m$) disorder to defect fluorite ($Fm\bar{3}m$) via cation and anion disordering. Total scattering experiments with sensitivity to the cation and anion sublattices provide unique insight into the underlying atomic processes. Using simultaneous Rietveld refinement (long-range structure) and small-box refinement PDF analysis (short-range structure), we show that the series undergoes a rapid transformation from pyrochlore to defect fluorite at $x \approx 1.2$, while the short-range structure exhibits a linear increase in a local weberite-type phase, $C222_1$, over the entire composition range. Enthalpies of formation from the oxides $\Delta H_{f,ox}^{\circ}$ determined using high temperature oxide melt solution calorimetry support the structural data and provide insight into the effect of local ordering on the energetics of disorder. The measured enthalpies of mixing are negative and are fit by a regular solution parameter of $W = -31.8 \pm 3.7$ kJ mol^{-1}. However, the extensive short-range ordering determined from the structural analysis strongly suggests that the entropies of mixing must be far less positive than implied by the random mixing of a regular solution. We propose a local disordering scheme involving the pyrochlore 48f to 8a site oxygen Frenkel defect that creates 7-coordinated Zr sites contained within local weberite-type coherent nanodomains. Thus, the solid solution is best described as a mixture of two phases, with the weberite-type nanodomains triggering the long-range structural transformation to defect fluorite after accumulation above a critical concentration (50% Ti replaced by Zr).

1. Introduction

Defect formation, defect mobility, and associated disorder profoundly affect the physical properties of many materials and affect material performance in both ambient and extreme environments. As a result, there is a need for a better

[a]*Department of Nuclear Engineering, University of Tennessee, Knoxville, TN, 37996, USA. E-mail: mlang2@utk.edu*

[b]*School of Molecular Sciences, Center for Materials of the Universe, Arizona State University, Tempe, AZ, 85287, USA*

[c]*Laboratoire Structures, Propriétés et Modélisation des Solides, CNRS, Centrale Supélec, Université Paris-Saclay, F-91190 Gif-sur-Yvette, France*

[d]*Cinvestav Unidad Saltillo, 25900 Ramos Arizpe, Coahuila, Mexico*

[e]*Neutron Scattering Division, Oak Ridge National Laboratory, Oak Ridge, TN, 37831, USA*

[f]*Department of Materials Science and Chemical Engineering, State University of New York, Stony Brook, NY, 11794, USA*

[g]*Department of Geological Sciences, Stanford University, Stanford, CA, 94305, USA*

understanding of order–disorder transformations in these technologically important materials. Pyrochlore oxides with general formula $A_2B_2O_7$ have exceptional chemical versatility and structural flexibility,[1-6] as well as unique defect dynamics,[6-12] that have made pyrochlore structures the center of investigation for a wide variety of energy related applications. Some pyrochlore compounds exhibit useful properties such as catalytic activity, piezoelectricity, ferro- and ferrimagnetism, luminescence, and giant magnetoresistance.[1,4,13,14] The electronic properties of pyrochlores vary from being superconducting, metallic, or semiconducting to having a high ionic conductivity.[4,13] Pyrochlore compositions are being developed for use as electrolytes in solid oxide fuel cells,[9,15] thermal barrier coatings (TBCs) for high wear/high temperature components,[16] oxygen gas sensors,[17] and nuclear waste forms for the immobilization of Pu and other actinides.[2,7,18-20]

The ideal fully ordered cubic pyrochlore structure (Fig. 1a) is given by the formula $A_2B_2X_6YZ$ with A and B being cations, X
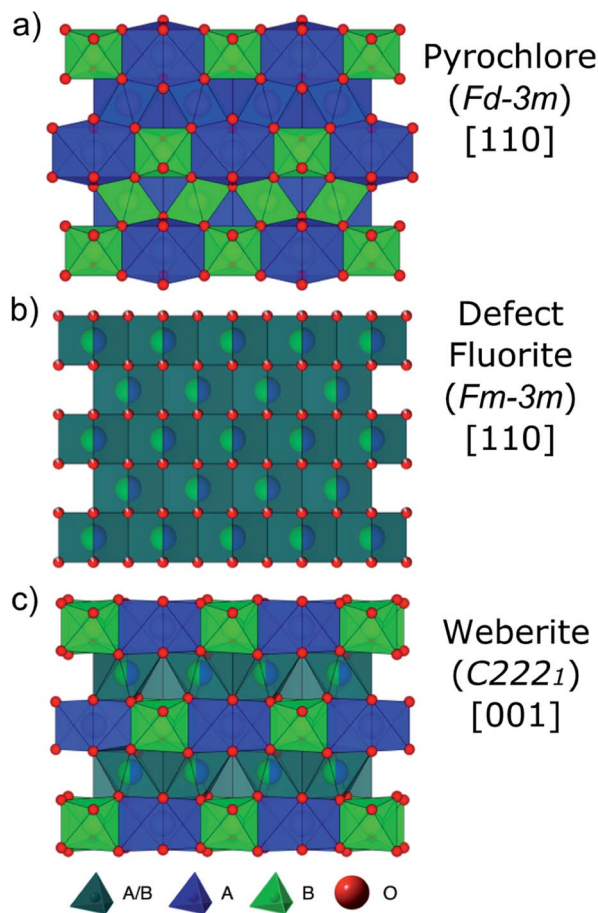
Fig. 1 Structural representations of (a) $A_2B_2O_7$ fully-ordered pyrochlore ($Fd\bar{3}m$) viewed down [110], (b) $A_{0.5}B_{0.5}O_{1.75}$ disordered, defect fluorite ($Fm\bar{3}m$) viewed down [110], and (c) $A_2B_2O_7$ partially ordered weberite-type ($C222_1$) viewed down [001]. A-site cations and their coordination polyhedra are represented in blue, B-site cations in green, and mixed A/B-site cations in gray. Red spheres are oxygen anions, with (b) partial spheres representing partially occupied sites.

and Y anions, and Z a constitutional vacancy ($Fd\bar{3}m$). Pyrochlore is a $2 \times 2 \times 2$ superstructure of the fluorite unit cell AX_2 ($Fm\bar{3}m$) with two cation sites and three anion sites containing one-eighth fewer anions (M : X ratio 4 : 7 *vs.* 1 : 2).[21,22] The eight-coordinated A-site (16d) is occupied by the larger cation, often a trivalent rare earth element with ionic radius $\sim$1 Å,[23] and the six-coordinated B-site (16c) by the smaller cation, usually a tetravalent 3d, 4d, or 5d transition metal or IVa group element with ionic radius $\sim$0.6 Å.[23] Oxygen atoms occupy the X (48f) and Y (8b) sites with constitutional vacancies on the Z (8a) site. The presence of multiple cations with different valences drives the cations to order themselves in the structure. The coordination environments of the cations are AX_6Y_2 and BX_6Z_2, while the anions are each coordinated by four cations (XA_2B_2, YA_4, and ZB_4). This structure is highly symmetric, with the free parameters being the unit-cell parameter (a) and the 48f anion x-position (x_{48f}).

The ordered pyrochlore structure (*e.g.*, $Ho_2Ti_2O_7$, Fig. 1a) is susceptible to disordering, which proceeds over the longer length scales by randomization of the cation and anion

sublattices and results in a disordered, defect fluorite structure (*e.g.*, $Ho_2Zr_2O_7$, Fig. 1b).[8] The A- and B-site coordination number (CN) changes from 8 and 6 in pyrochlore, respectively, to on average 7 for both. This order–disorder transformation can be induced by chemical substitution (achieved *via* synthesis/doping),[24,25] temperature or pressure,[10,24,26] or ion irradiation.[26,27] Whether a pyrochlore composition disorders to defect fluorite, or not, has been shown to be predominantly controlled by the energetics of defect formation and disordering.[7,28,29] The propensity for antisite defects (A and B cation exchange) to form is strongly correlated with the A and B cation radii ratio, r_A/r_B.[1,3,7,12,19,30] If cation radii are similar ($r_A/r_B < 1.46$), formation of antisite defects is more energetically favorable and the disordered, defect fluorite atomic arrangement is preferred.

The effect of direct chemical substitution of the B-site cation on the pyrochlore-to-defect fluorite transformation has been studied extensively using a variety of solid solution series, such as $Y_2B_{2-x}B'_xO_7$ (B and B$'$ = Ti, Sn, or Zr, B $\neq$ B$'$) and Ho_2-$Ti_{2-x}Zr_xO_7$.[9,15,24,25,31–36] These studies utilized X-ray and neutron diffraction to probe the long-range structure and used X-ray absorption spectroscopy to probe short-range effects, observing how disordering proceeds as a function of chemical composition. Probing the local structure of $Y_2B_{2-x}Zr_xO_7$ (B = Ti or Sn) pyrochlore compounds using Raman and NMR spectroscopy confirms a gradual order–disorder transition from pyrochlore to defect fluorite with increasing Zr-content.[33–35,37] Additional spectroscopic studies using Raman, magic-angle spinning nuclear magnetic resonance (MAS NMR), and X-ray absorption near-edge structure (XANES), supported by density functional theory (DFT) calculations, have revealed short- and intermediate range compositional and structural modulations that indicate retention of pyrochlore-like ordering well into the Zr-rich defect fluorite phase.[38,39] Utilizing diffraction methods, Wuensch et al.[9,15,24,32] and Shafique et al.[36] reported that the $Y_2Sn_{2-x}Zr_xO_7$, $Y_2Ti_{2-x}Zr_xO_7$, and $Ho_2Ti_{2-x}Zr_xO_7$ solid solution series disorder progressively with increasing Zr-content, with disorder on the cation and anion sublattices proceeding at different rates and seemingly independently. As Zr replaces Ti or Sn, oxygen anions from 48f sites, and later the 8b sites at higher fractions of Zr, begin to occupy the vacant 8a sites. The cation sublattice remains ordered until the Zr-content reaches more than 50% ($x = 1.0$), at which point the exchange of A and B site cations occurs much more efficiently. The differences in disordering behavior on each sublattice is even larger for Y_2-$Sn_{2-x}Zr_xO_7$, with only 31% of Sn occupying the A-site at $x = 1.6$ while the anions are nearly fully disordered. In both the Y_2-$Ti_{2-x}Zr_xO_7$ and $Y_2Sn_{2-x}Zr_xO_7$ systems, the anion sublattice disorders before the cation sublattice, and the complete transition to defect fluorite is not attained until the Zr-content is substantial ($x > 1.6$).

Studies of disordered pyrochlores over the past two decades suggest that the short-range structure is more ordered than is implied by the observable long-range defect fluorite structure.[25,31,35,40,41] Recent studies using neutron total scattering experiments with pair distribution function (PDF) analysis of disordered pyrochlore (*e.g.*, $Ho_2Zr_2O_7$) have uncovered that the local atomic arrangement of the defect fluorite phase is actually

described by a partially ordered orthorhombic phase,[42] the structure of which can be described by a weberite-type ($C222_1$) structural model that is isostructural to Y_3TaO_7.[42–47] The weberite-type structure is another derivative of the fluorite structure with a $2 \times \sqrt{2} \times \sqrt{2}$ superstructure that contains a higher degree of ordered arrangements of different valence cations and ordered anion vacancies as compared with defect fluorite but is distinct from pyrochlore (Fig. 1c). In a weberite-type structure, the cation sublattice is split unequally into three cation sublattices, with the trivalent cation occupying the eight-coordinated 4b sites, the tetravalent cation occupying the six-coordinated 4b sites, and both cations occupying the seven-coordinated 8c sites randomly. The anions are distributed onto two sets of 8c sites and three sets of 4c sites, with constitutional vacancies on additional 4c sites. The general formula for weberite can be written as $ABC_2X_4Y_2Z$. Compounds that exhibit the long-range weberite structure display a pronounced chemical selectivity. A recent computational study by Solomon *et al.* shows that low-energy, long-range weberite-type configurations are favored at low values of the ionic radius ratio of A- and B-site cations r_A/r_B.[48] Random averaging of weberite-type local configurations leads to a long-range disordered, defect fluorite structure when averaged over many unit cells.[44,46] Heterogeneous disordering processes with different short- and long-range structural motifs have been similarly observed for other ceramics, such as spinel,[49] and different disordering processes through intrinsic (nonstoichiometry and chemical composition[15,50]) and extrinsic (ball milling and irradiation[43,51]) means. This behavior is consistent with Pauling's rules which have been shown to dictate the local atomic arrangements in disordered ceramics.[46]

In addition to structural and computational evidence of short-range ordering in disordered pyrochlore, thermodynamic data obtained by Navrotsky and coworkers using high temperature oxide melt solution calorimetry suggests the occurrence of short-range ordering in disordered pyrochlore,[40,41] the fluorite related ZrO_2–RE_2O_3, HfO_2–RE_2O_3, and CeO_2–RE_2O_3 (RE = rare earth) solid solutions,[52–57] and recently in the zircon $Th_{1-x}U_x$-SiO_4 solid solution.[58] The finding of weberite-type short-range ordering in nominally disordered pyrochlores by Shamblin *et al.*[42] has led to many thermodynamic studies aimed at understanding the mechanism and energetics of order–disorder transitions in pyrochlores, weberites, and other compounds with fluorite-derived structures.[52,59–62]
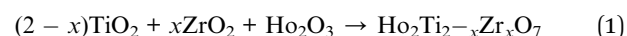
While the local atomic arrangement and long-range structure in fully disordered complex oxides has been studied in detail, little information is available on the behavior at both length scales in partially disordered materials. In this study, neutron and X-ray total scattering experiments were performed on nine members of the solid solution series $Ho_2Ti_{2-x}Zr_xO_7$ ($0 \leq x \leq 2.0$) to comprehensively characterize the chemically induced order–disorder transformation across both short and long length scales. Analysis of the PDFs and structure functions provides insight into the role that specific local defects (and associated correlated disorder) play in the long-range order–disorder transformation. The scattering experiments were complemented by oxide melt solution calorimetry to determine enthalpies of formation (ΔH_f) and mixing (ΔH_{mix}) of the solid solution series. Both structural and thermodynamic results provide strong evidence for a complex short-range ordering scheme that drives the long-range behavior observable by conventional diffraction analysis.

2. Methods

2.1 Sample synthesis

Polycrystalline samples of $Ho_2Ti_{2-x}Zr_xO_7$ ($x = 0.0, 0.25, 0.5, 0.75, 1.0, 1.25, 1.5, 1.75,$ and 2.0) were synthesized using standard solid-state techniques. High purity reagent oxides (TiO_2, ZrO_2 and Ho_2O_3) were purchased from Sigma-Aldrich and mixed *via* the following solid-state reaction:

$$(2-x)TiO_2 + xZrO_2 + Ho_2O_3 \rightarrow Ho_2Ti_{2-x}Zr_xO_7 \qquad (1)$$

The powders were mixed thoroughly in an agate mortar and were uniaxially pressed into pellets in a hydraulic press with a pressure of 315 MPa, resulting in pellets 1 cm in diameter and approximately 2–3 mm thick. The pellets were subsequently fired in air at 1500 °C for 72 hours, with intermediate grinding and pressing every 12 hours. The pellets were allowed to cool at the natural cooling rate of the furnace following each firing cycle. After the final firing/cooling cycle, the pellets were hand-ground into a fine powder for use in neutron and X-ray total scattering experiments. The resulting powders were all a light pink-orange color, darkening very slightly with increasing x.

2.2 Neutron and X-ray total scattering measurements

Neutron total scattering measurements were performed at the Nanoscale Ordered Materials Diffractometer (NOMAD) beamline at the Spallation Neutron Source (SNS),[63] located at Oak Ridge National Laboratory (ORNL). NOMAD's high intensity neutron beam combined with a large accessible momentum transfer range and good momentum transfer resolution make it ideal for the study of disordered, low-mass samples. Approximately 200 mg of each composition were loaded into quartz capillaries with diameters of 2 mm and wall thicknesses of 0.01 mm. Measurements of diamond and silicon powders were used to calibrate NOMAD's time-of-flight detector banks and to determine instrument parameters for use in structural refinement software. NOMAD's detection system consists of six banks of over 300 ^{3}He linear position sensitive detectors that can routinely reach maximum momentum transfer values of 50 Å^{-1} and greater. Each sample and an empty quartz capillary were measured for approximately 60 minutes at room temperature. The total scattering structure functions, $S(Q)$, were produced by combining diffraction data from all six banks and after background subtraction (from the empty quartz capillary) and normalization of the sample scattering intensity to the scattering intensity from a solid vanadium rod. The pair distribution functions, $G(r)$, were obtained through the Fourier transform of $S(Q)$ with $Q_{min} = 0.2$ Å^{-1} and $Q_{max} = 31.4$ Å^{-1}:

Paper

$$G(r) = r \left(A \int_{Q_{\min}}^{Q_{\max}} Q[S(Q) - 1]\sin(Qr)\mathrm{d}Q \right) \quad (2)$$

where r is the real-space distance in Å, A is an arbitrary scaling factor, and Q is the scattering vector, defined as:

$$Q = \frac{4\pi \sin \theta}{\lambda}, \quad (3)$$

with λ representing the neutron wavelength and θ the scattering angle. A Lorch function was applied to the neutron PDFs to reduce the intensities of truncation ripples.[64]

X-ray total scattering characterization was performed at the 28-ID-2 (XPD) beamline at the National Synchrotron Light Source-II (NSLS-II)[65,66] at Brookhaven National Laboratory (BNL). All nine series members' powders were placed in Kapton tube capillaries with an outer diameter of 1.11 mm and a wall thickness of 50.8 μm which serve as sample containers. The capillaries were filled to a height of 3.0 cm with sample powder and sealed with approximately 0.5 cm long polymer stoppers inserted into both ends. Measurements of a LaB₆ 660a standard powder were used for the calibration of XPD's 2D detector and to determine the instrument parameters for use in structural refinement software. All measurements were performed at room temperature with an exposure time of 10 seconds per sample and photon wavelength of 0.18754 Å (~66.1 keV). An empty Kapton tube as well as a LaB₆ standard were measured to correctly subtract the capillary's scattering contribution as background and properly scale each sample's scattering intensity. The X-ray scattering from each sample was recorded as 2D diffractograms gathered using a PerkinElmer XRD 1621 digital imaging detector with an active area of $16'' \times 16''$ and resolution of 2048×2048 pixels which in XPD's detector setup can collect reasonably good quality data up to maximum momentum transfer values of 27.0 Å⁻¹. Resulting 2D diffraction images were transformed into structure functions $S(Q)$, with the scattering vector Q varying from $Q_{\min} = 0.5$ Å⁻¹ to $Q_{\max} = 25.0$ Å⁻¹. Pair distribution functions, $G(r)$, were obtained through eqn (2) using the software PDFgetX3.[67] Unlike the neutron PDFs, no Lorch function was applied to the X-ray PDFs as the first few peaks, where truncation ripples are most prominent, were not used in the small-box refinements of these PDFs.

2.3 Structure data analysis

The long-range structure Rietveld refinements of neutron and X-ray data were performed using the GSAS-II software package.[68] Structural refinement of the measured Ho₂Ti₂₋ₓZrₓO₇ samples were performed using the $Fd\bar{3}m$ and/or $Fm\bar{3}m$ space group (Table 1), depending on which space group fit the diffraction pattern best. For the $Fd\bar{3}m$ structural model, the unit cell parameter a_P and the 48f anion x-position x_{48f} were refined. All three oxygen sites (48f, 8b, and 8a) occupancies n_i were refined. To maintain oxygen balance among the three sites, the occupancies were constrained using the following relation:

$$48n_{48f} + 8n_{8b} + 8n_{8a} = 56 \quad (4)$$

Table 1 Initial structure models used in Rietveld refinements and small-box refinements[a]

Wyckoff equipoint (CN)	Occupancy	x	y	z
$Fd\bar{3}m$ (pyrochlore, space group no. 227)				
16d (8)	Ho	0.5	0.5	0.5
16c (6)	Ti$_{1-x/2}$Zr$_{x/2}$	0	0	0
48f	O$_{(1-i)/6}$	**0.3317**	0.125	0.125
8b	O′	0.375	0.375	0.375
8a	O$_i$	0.125	0.125	0.125
$Fm\bar{3}m$ (defect fluorite, space group no. 225)				
4a (7)	Ho$_{0.5}$Ti$_{x/4}$Zr$_{1-x/4}$	0	0	0
8c	O$_{0.875}$	0.25	0.25	0.25
$C222_1$ (weberite, space group no. 20)				
4b (8)	Ho	0	**0.4956**	0.25
8c (7)	Ho$_{1/2}$Zr$_{1/2}$	**0.2360**	**0.2374**	0
4b (6)	Zr	0	**0**	0.25
8c	O	**0.139**	**0.181**	**0.304**
8c	O	**0.121**	**0.770**	**0.267**
4a	O	**0.131**	0.5	0
4a	O	**0.131**	0.5	0.5
4a	O	**0.072**	0	0

[a] Free parameters are in bold.

This accounts for oxygen anions shifting from the occupied 48f and 8b sites to the vacant 8a site. The isotropic thermal parameters for the 8b and 8a oxygen sites were refined to be equal ($u_{8b} = u_{8a}$). The cation sublattice was constrained to have fully occupied sites. For the $Fm\bar{3}m$ structural model, the unit cell parameter, a_{DF}, was refined. The distribution of the three atomic species (Ho, Ti, Zr) over the two crystallographically distinct A- and B-sites in $Fd\bar{3}m$ cannot be uniquely determined from diffraction experiments alone; rather, it is only possible to determine the average scattering lengths of each site with the added limitation of reasonable isotropic thermal parameters, with the highest thermal parameter refined for all fits being approximately 0.04 for the 8c oxygen site. This is further complicated by the somewhat similar neutron scattering lengths of Ho and Zr (Table 2). Therefore, it was assumed for the pyrochlore fits that Ho fully occupies the A-site and not the B-site and *vice versa* for Ti and Zr, though Ti and Zr occupancies on the B-site were allowed to vary with changing Zr-content to match the stoichiometry of each sample. For both space group refinements, the isotropic thermal parameters were refined independently, with the exception of the 8b and 8a sites in the $Fd\bar{3}m$ refinements. The background was fitted using a shifted, 16-term Chebyshev polynomial.

In GSAS-II, a "background" can be defined to be subtracted from diffraction patterns. Normally diffuse scattering is discarded with this background. However, the diffuse scattering changes with composition and provides additional information on the short- and medium-range behaviors beyond the PDF analysis. To subtract the background associated with the measurement and retain the diffuse scattering from the sample, the fully ordered pyrochlore Ho₂Ti₂O₇ endmember was assumed to have no diffuse scattering. The refined background

Table 2   Ionic radii, neutron scattering lengths, and X-ray scattering lengths for various ions

Element/ion	Ionic radius (Å)[23]	Neutron scattering length (b_{ni}) (fm)[69]	X-ray scattering length $(b_{xi} = r_e f_1)^{a,b}$ (fm)[70]
Ho^{3+}	0.901 (VI)	8.01	187.8
	1.015 (VIII)		
Zr^{4+}	0.72 (VI)	7.16	112.9
	0.78 (VII)		
	0.84 (VIII)		
Ti^{4+}	0.605 (VI)	−3.44	62.2
	0.74 (VIII)		
O^{2-}	1.38 (IV)	5.80	22.6

[a] Classical electron radius r_e; real part of the atomic scattering factor f_1.
[b] X-ray energy of 66.1 keV.

polynomial for this composition was then used as universal background associated with the measurement (with slight modifications to account for peak position shifts for the different chemical compositions). Rietveld refinement was then repeated with the previously determined structural models but with the new background polynomial. The subsequent increase in the goodness-of-fit (R_w) parameter was then used as a measure of the impact that diffuse scattering has on the quality of the fit.

Local structure characterizations were obtained from small-box refinements of the PDFs using the software package PDFgui.[71] The small-box refinements were performed using: (i) the cubic $Fd\bar{3}m$ structure, (ii) the orthorhombic weberite $C222_1$ structure, and (iii) a local two-phase mixed structural model consisting of (i) and (ii).

Nine parameters were refined for the fully ordered pyrochlore endmember, $Ho_2Ti_2O_7$, with cubic $Fd\bar{3}m$ symmetry: the unit cell parameter ($a = b = c$), the scale factor, the linear correlated motion factor, atomic displacement parameters (ADPs) for the 16c, 16d, and 8b sites ($u_{11} = u_{22} = u_{33}$), the x-position for the 48f site, and the ADPs for the 48f site ($u_{11} \neq u_{22} = u_{33}$). The anisotropic ADPs for the 16c and 16d sites ($u_{12} = u_{23} = u_{13}$) and the 48f site ($u_{23} \neq 0$) were fixed. Thirty-three parameters were refined for the fully disordered endmember, $Ho_2Zr_2O_7$, with orthorhombic $C222_1$ symmetry (weberite-type): the unit cell parameters ($a \neq b \neq c$), the scale factor, the linear correlated motion factor, the ADPs for the two 4b sites ($u_{11} = u_{22} = u_{33}$), the ADPs for the three 8c sites and three 4a sites ($u_{11} \neq u_{22} \neq u_{33}$), the y-positions for the two 4b sites, the x-, y-, and z-positions for the three 8c sites, and the x-positions for the three 4a sites. It is more correct to model the system as harmonic (refining u_{12}, u_{23}, u_{13} where appropriate), but this was forgone in favor of a more isotropic treatment of the ADPs to simplify the model and improve convergence of the calculations. The two-phase model used for the intermediate compositions retained the same parameters listed for the two endmember models, but with the addition of a weberite-type phase fraction parameter, totaling 49 parameters. All refinements resulted in no highly correlated parameters.

To study the R_{wp} values of the $Fd\bar{3}m$ and $Fm\bar{3}m$ models to the local structure, PDF "boxcar" refinements were performed. PDF small-box refinements were carried out in the 1.7–11.7 Å r-range using the structural parameters found during Rietveld refinement as the initial parameters. Once the R_{wp} for that range was obtained, successive 10 Å refinements were repeated in progressively higher r-space, with the final values of each refinement becoming the initial parameters of the next fitting, like train "boxcars". The goodness of fit in PDFgui is defined as

$$R_{wp} = \sqrt{\frac{\sum_{i=1}^{N} w(r_i)[G_{obs}(r_i) - G_{calc}(r_i)]^2}{\sum_{i=1}^{N} w(r_i)[G_{obs}(r_i)]^2}} \quad (5)$$

where $w(r_i)$ is the weight of data point r_i, $G_{obs}(r_i)$ is the experimentally observed data point, and $G_{calc}(r_i)$ is the calculated data point. Values of R_{wp} less than 20% are considered generally acceptable for most crystalline materials.[72,73] Q_{damp} and Q_{broad} for the PDF refinements were determined using the PDFs of diamond powder and LaB_6 powder standards for neutron and X-ray PDFs, respectively.

An approach developed by Neder et al. allows for the modelling of the diffuse scattering observed in the structure functions, $S(Q)$, by including the contributions of coherent nanodomains to the scattering.[74] This approach splits the overall diffracted intensity into the sum of two contributions: (i) a long-range average structure, where the atoms have weighted occupancies from averaging all nanodomain variants, and (ii) a "difference" structure, where the atom occupancies and positions account for the difference between the nanodomain ordered structure and the long-range configurational average. A Scherrer-type finite size broadening was used to describe the broadening produced by the finite correlation length of the nanodomain structure and the spatial average extension of the correlation giving rise to diffuse scattering. The Rietveld software GSAS-II was used to implement this approach and scattering data gathered with NOMAD detector bank 2 was chosen for fitting to best capture both the Bragg and the diffuse scattering.

2.4   High temperature oxide melt solution calorimetry

High temperature calorimetry was performed using a Tian Calvet twin-calorimeter AlexSYS (Setaram, Cailure, France) to determine the enthalpies of formation $\Delta H_{f,ox}^{\circ}$ of all nine members of the $Ho_2Ti_{2-x}Zr_xO_7$ solid solution series. The solvent used was sodium molybdate ($3Na_2O \cdot 4MoO_3$) prepared according to ref. 75 using MoO_3 (Fisher, 99.5% purity) and $Na_2MoO_4 \cdot 2H_2O$ (Emdmillipore, 99.5% purity) as reagents. The calorimeter was calibrated against the heat content of 5 mg pellets of α-Al_2O_3.[76] Sample powders were preheated to 800 °C for 8 hours to remove potential residue water, pressed into 5–8 mg pellets, and dropped at room temperature into a platinum crucible containing 20 g of molten solvent at 800 °C. A constant flow rate of O_2 was flushed over the solvent at 90 ml min⁻¹ to create a stable environment above the solvent and bubbled through it at 5 ml min⁻¹ to ensure an oxidative environment.[76]
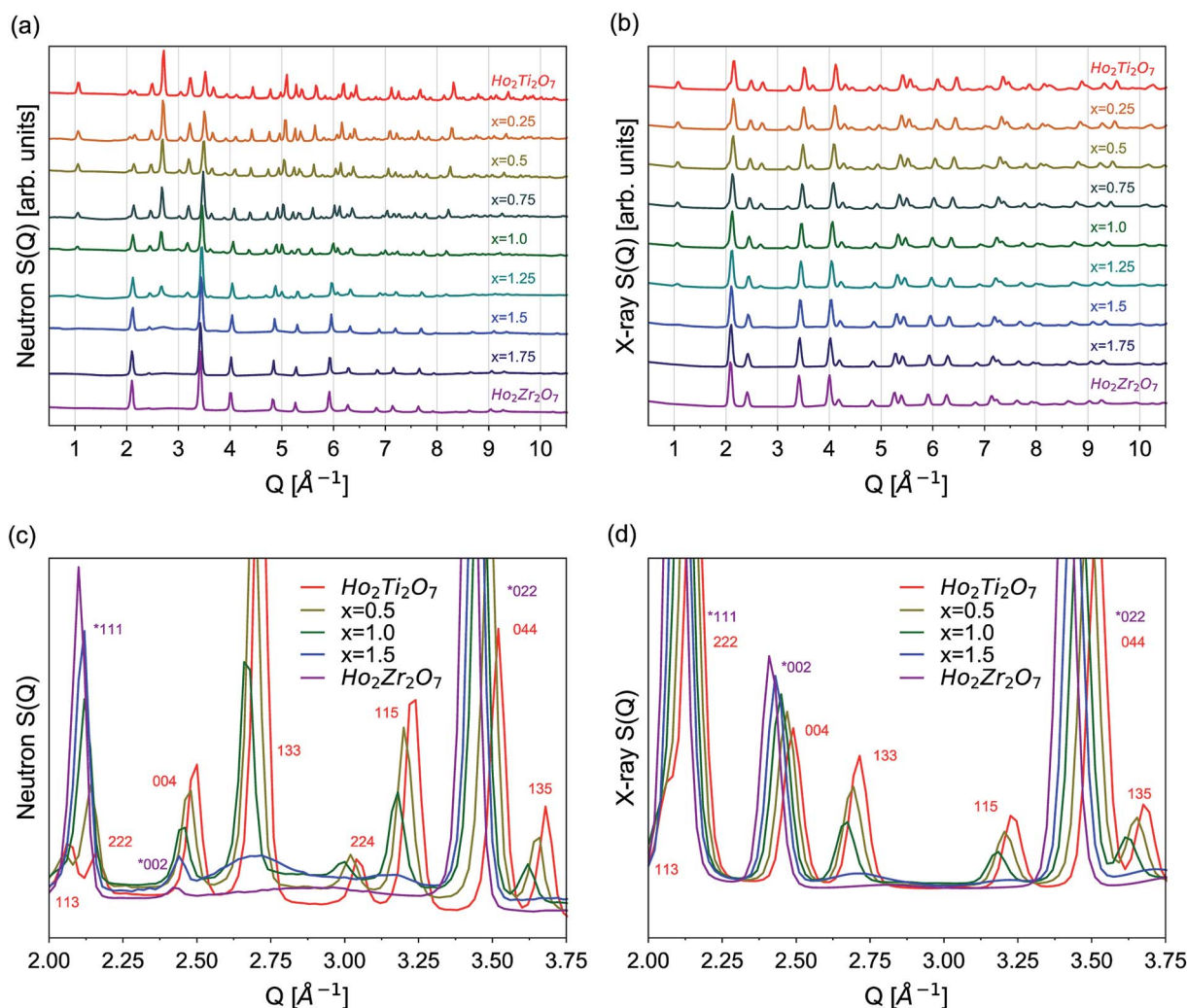
Paper

Table 3 Thermochemical cycle for the calculation of enthalpy of formation for $Ho_2Ti_{2-x}Zr_xO_7$ ($0 \leq x \leq 2.0$) in $3Na_2O \cdot 4MoO_3$ solvent at 800 °C

Reaction		ΔH (kJ mol^{-1})
$Ho_2Ti_{2-x}Zr_xO_{7(s,25)} \rightarrow Ho_2O_{3(sln,800)} + (2-x)TiO_{2(sln,800)} + xZrO_{2(sln,800)}$	{1} ΔH_{ds} – $Ho_2Ti_{2-x}Zr_xO_7$	Table 7
$Ho_2O_{3(s,25)} \rightarrow Ho_2O_{3(sln,800)}$	{2} ΔH_{ds} – Ho_2O_3	-109.4 ± 1.8^a
$TiO_{2(s,25)} \rightarrow TiO_{2(sln,800)}$	{3} ΔH_{ds} – TiO_2	73.4 ± 0.4^b
$ZrO_{2(s,25)} \rightarrow ZrO_{2(sln,800)}$	{4} ΔH_{ds} – ZrO_2	29.2 ± 1.6^c
$Ho_2O_{3(s,25)} + (2-x)TiO_{2(s,25)} + xZrO_{2(s,25)} \rightarrow Ho_2Ti_{2-x}Zr_xO_{7(s,25)}$	{5} $\Delta H^\circ_{f,ox}$ – $Ho_2Ti_{2-x}Zr_xO_7$	Table 7
$\Delta H\{5\} = -\Delta H\{1\} + \Delta H\{2\} + (2-x)\Delta H\{3\} + x\Delta H\{4\}$		

^{a} Ref. 76. ^{b} Ref. 80. ^{c} Measured as part of this work, s = solid, sln = solution, ds = drop solution, f,ox = formation from oxides, 25 = 25 °C, and 800 = 800 °C.

The enthalpy of drop solution, ΔH_{ds}, which is the measured heat effect of dropping a room temperature pellet into the solvent and is the sum of the heat content of the sample and the heat released during its dissolution, was calculated by integrating the heat flow curve using CALISTO software provided by Setaram. This procedure and methodology have been used extensively on other similar materials and described in detail previously.[76–79] The thermochemical cycle used for the calculation of the enthalpies of formation, $\Delta H^\circ_{f,ox}$, from ΔH_{ds} are summarized in Table 3. The needed ΔH_{ds} values for Ho_2O_3 and

Fig. 2 (a) Neutron and (b) X-ray total scattering structure functions, $S(Q)$, from 0.5 Å^{-1} to 10.5 Å^{-1} for the complete $Ho_2Ti_{2-x}Zr_xO_7$ series. (c) Neutron and (d) X-ray overlays of select series members' structure functions (x = 0.0, 0.5, 1.0, 1.5, 2.0) from 2.0 Å^{-1} to 3.75 Å^{-1}. Indices for pyrochlore, $Fd\bar{3}m$, are given in red and indices for defect fluorite, $Fm\bar{3}m$, are given in purple and marked with an asterisk (*).

TiO_2 were acquired from literature ref. 76 and 80, respectively, and that of ZrO_2 was measured in this study. Up to 8 drops were performed for each sample to reduce the uncertainty in the measurement.

3. Results

3.1 Long-range structure – neutron and X-ray reciprocal space analysis

The as-collected neutron and X-ray structure functions for all $Ho_2Ti_{2-x}Zr_xO_7$ compositions are shown in Fig. 2. The structure functions indicate that the samples are well-crystallized, and no detectable peaks associated with impurities are present. A gradual shift in common Bragg peaks to lower Q marks the expansion of the unit cell with increasing Zr-content, x. Disorder of the cation and anion sublattices across the series is observed as distinct changes in the relative intensities of various Bragg peaks. Disordering of the cation sublattice results in pyrochlore superstructure diffraction peaks with odd Miller indices to have reduced intensities across the entire Q-range (e.g., (111), (113), (133), (115), and (135)). Conversely, most pyrochlore diffraction peaks with even Miller indices exhibit marked increases in intensities (e.g., (222) and (044)). The disappearance of most superstructure peaks is consistently observed in the neutron and X-ray diffraction patterns between

$x = 1.25$ and 1.5, indicating the total conversion from ordered pyrochlore to disordered, defect fluorite. This behavior is in agreement with previous diffraction studies on the $Ho_2Ti_{2-x}Zr_xO_7$ and $Y_2B_{2-x}Zr_xO_7$ (B = Ti or Sn) solid solution series.[15,25,35,36] Disordering of the anion sublattice is complex and is more effectively observed using neutrons, as neutron total scattering is sensitive to the oxygen sublattice. Neutron scattering lengths, unlike X-ray scattering lengths, are independent of the number of electrons around the ion, making some diffraction peaks associated to the oxygen sublattice highly visible to neutrons, e.g., (224) in Fig. 2c and d. In some cases, neutrons are also able to discern the different species of cations better than X-rays (e.g., Zr and Ti) (Table 2).

Rietveld refinements were performed on all neutron and X-ray diffraction patterns using the pyrochlore ($Fd\bar{3}m$) and/or defect fluorite ($Fm\bar{3}m$) structural models described in Table 1. Refinements of the endmembers yielded structural parameters that are in agreement with previous neutron scattering studies,[36,42] with the long-range structure of $Ho_2Ti_2O_7$ being best described as an ordered pyrochlore structure and $Ho_2Zr_2O_7$ by a fully disordered, defect fluorite structure. For the intermediate compositions, the pyrochlore structure best fit the diffraction patterns for the compositions $x = 0.25$, 0.5, and 0.75, while the disordered, defect fluorite was the best fit for the compositions $x = 1.5$, 1.75, and 2.0. Both phases were found to coexist at $x =$

Table 4 Refined parameter values and uncertainties for Rietveld refinements

Neutron Rietveld refinement (fit range $Q = 3.3–14.2$ Å^{-1})

Composition	Structure	$Fm\bar{3}m$ fraction, f	a [Å]	x_{48f}	n_{8a}	R_w (%) $-DS^d$	R_w (%) $+DS^d$
$Ho_2Ti_2O_7$	$Fd\bar{3}m$	0	10.1013(2)	0.3289(1)	0	5.81	5.81
$Ho_2Ti_{1.75}Zr_{0.25}O_7$	$Fd\bar{3}m$	0	10.1469(2)	0.3300(1)	0.03(1)	6.03	6.16
$Ho_2Ti_{1.50}Zr_{0.50}O_7$	$Fd\bar{3}m$	0	10.1871(3)	0.3324(2)	0.10(1)	5.57	5.73
$Ho_2Ti_{1.25}Zr_{0.75}O_7$	$Fd\bar{3}m$	0	10.2300(2)	0.3348(2)	0.12(1)	5.74	5.96
$Ho_2Ti_{1.00}Zr_{1.00}O_7$	$Fd\bar{3}m + Fm\bar{3}m$	0.026(2)	10.2725(4)	0.3395(3)	0.20(6)	5.00	5.24
			5.160(7)	0.375[a]	0.875[b]		
$Ho_2Ti_{0.75}Zr_{1.25}O_7$	$Fd\bar{3}m + Fm\bar{3}m$	0.80(3)	10.284(1)	0.3380(5)	0.09(4)	5.55	6.43
			5.1593(3)	0.375[a]	0.875[b]		
$Ho_2Ti_{0.50}Zr_{1.50}O_7$	$Fm\bar{3}m$	1	5.1633(2)	0.375[a]	0.875[b]	7.20	9.10
$Ho_2Ti_{0.25}Zr_{1.75}O_7$	$Fm\bar{3}m$	1	5.1922(1)	0.375[a]	0.875[b]	7.31	11.92
$Ho_2Zr_2O_7$	$Fm\bar{3}m$	1	5.2289(3)[c]	0.375[a]	0.875[b]	7.98	9.62

X-ray Rietveld refinement (fit range $Q = 0.8–25$ Å^{-1})

Composition	Structure	$Fm\bar{3}m$ fraction, f	a_0 [Å]	x_{48f}	8a site fraction	R_w (%)
$Ho_2Ti_2O_7$	$Fd\bar{3}m$	0	10.1024(4)	0.330(1)	0	1.76
$Ho_2Ti_{1.75}Zr_{0.25}O_7$	$Fd\bar{3}m$	0	10.1422(3)	0.334(1)	0	1.20
$Ho_2Ti_{1.50}Zr_{0.50}O_7$	$Fd\bar{3}m$	0	10.1857(4)	0.339(1)	0.06(7)	1.40
$Ho_2Ti_{1.25}Zr_{0.75}O_7$	$Fd\bar{3}m$	0	10.2266(5)	0.340(2)	0.12(7)	1.57
$Ho_2Ti_{1.00}Zr_{1.00}O_7$	$Fd\bar{3}m$	0	10.2741(6)	0.341(2)	0.28(9)	1.68
$Ho_2Ti_{0.75}Zr_{1.25}O_7$	$Fd\bar{3}m + Fm\bar{3}m$	0.73(4)	10.273(2)	0.345(3)	0	1.75
			5.1588(6)	0.375[a]	0.875[b]	
$Ho_2Ti_{0.50}Zr_{1.50}O_7$	$Fm\bar{3}m$	1	5.1703(4)	0.375[a]	0.875[b]	2.48
$Ho_2Ti_{0.25}Zr_{1.75}O_7$	$Fm\bar{3}m$	1	5.1918(3)	0.375[a]	0.875[b]	2.07
$Ho_2Zr_2O_7$	$Fm\bar{3}m$	1	5.2104(4)	0.375[a]	0.875[b]	2.38

[a] Equivalent x_{48f} in $Fm\bar{3}m$ is 0.375. [b] Equivalent n_{8a} in $Fm\bar{3}m$ is 0.875. [c] Two measurements were taken yielding a values 0.3% of each other. [d] Denotes whether the diffuse scattering was discarded with the background ($-DS$) or included in the refinement ($+DS$).

1.25 in both neutron and X-ray patterns and at $x = 1.0$ in the neutron pattern. The values obtained from refinements of all intermediate series members, including the defect fluorite $Fm\bar{3}m$ phase fraction, unit cell parameters, a, for both structures, refined 48f x-position parameter x_{48f}, 8a oxygen occupancy of the pyrochlore structure n_{8a}, and R_w values for each refinement, are summarized in Table 4. These parameters were found to agree acceptably with those of a previous neutron diffraction study.[36] A defect pyrochlore unit cell, where the 48f and 8b oxygens are allowed to shift and occupy the vacant 8a site, was found to best fit the diffraction patterns for the compositions $x = 0.25$, 0.5, 0.75, and 1.0. The x_{48f} and n_{8a} parameters increase across this range, a trend that is qualitatively similar to the behavior previously reported for the disordering processes in $Ho_2Ti_{2-x}Zr_xO_7$ and $Y_2B_{2-x}Zr_xO_7$ (B = Ti or Sn) solid solution series.[15,25,35,36] The x_{48f} parameter increases for x values up to 1.25 by 3.2% and 4.3% in the neutron and X-ray refinements, respectively. The parameter n_{8a} increases for x values up to 1.0 from 0 to 0.20 (neutrons) and from 0 to 0.28 (X-rays), which corresponds to 0, 1.6, and 2.24 out of 8 oxygen anions on the 8a site. Upon extensive formation of the defect fluorite structure at $x = 1.25$, the n_{8a} parameter drastically decreases to 0.09 (neutrons) and 0 (X-rays), corresponding to 0.72 oxygen anions. The 8b site remains fully occupied at all pyrochlore-containing compositions. For the mixed-phase compositions, the Ti and Zr occupancy levels in the defect fluorite phase were allowed to vary under the constraint of fully occupied cation sites. The refined defect fluorite phase was found to contain primarily Zr, with the Ti content increasing from 0% at $x = 1.0$, to approximately 7% at $x = 1.25$, to stoichiometric values at $x = 1.5$ where the pyrochlore phase was no longer evident in the structure functions and part of the structural refinement.

The change in unit cell parameter with respect to the pyrochlore endmember $Ho_2Ti_2O_7$ $\Delta a/a_{x=0}$ ($a = a_P$ and $2a_{DF}$) across the series exhibits a linear increase with increasing Zr-content, x, that resembles a trend following Vegard's law,[81] as expected from substituting the larger Zr cation for Ti (Fig. 3). There is a slight change in the slope of the unit cell parameters upon the phase change from pyrochlore to defect fluorite that deviates from Vegard's law. This behavior has been observed in other pyrochlore to defect fluorite solid solution series.[36,50,82] Linear fits through the neutron and X-ray data points reveal oversized defect fluorite and undersized pyrochlore unit cell parameters for the two-phase compositions at $x = 1.0$ and 1.25. When these two points are averaged using their corresponding phase fractions, the resulting unit cell parameters lie very close to the linear fits. The sample composition $x = 1.5$ has a slightly undersized unit cell parameter based on the neutron data, which may indicate the continued existence of a small amount of the pyrochlore phase beyond $x = 1.25$ or a small deviation from the x value.

Diffuse scattering is observed in the structure functions as background beneath and between the Bragg peaks, which is a result of short-range deviations from the long-range structure (Fig. 2c and d).[83] Increasing the Zr-content gradually to $x = 1.0$ increases the background baseline of the structure functions,

and broad, low intensity peaks are apparent for larger x values. This is particularly evident for the $x = 1.5$ composition as two broad peaks are observed between $Q = 2.5$ and 2.9 Å^{-1} and between $Q = 3.0$ and 3.3 Å^{-1}, approximately underneath the (133) and (115) peaks. The positions of the two new diffuse peaks do not follow the trend of the pyrochlore superlattice peaks, but rather adopt positions that are independent of the pyrochlore members. These two peaks merge into a single peak seen between $Q = 2.5$ and 3.3 Å^{-1} in the $Ho_2Zr_2O_7$ structure function. A consistent increase in diffuse scattering in the predominately pyrochlore members ($x = 0.0$ to 1.0) indicate that despite the pyrochlore long-range structure, local deviations from pyrochlore are increasingly present. Conversely, the diffuse scattering peaks in the disordered members ($x = 1.25$ to 2.0) signal local structural order that is distinct from defect fluorite. These trends are also observed at high Q where many small peaks merge with increasing x (not shown). The diffuse scattering is much more prominent in the neutron scattering patterns than the X-ray scattering patterns. The local ordering in the system is heavily influenced by the oxygen sublattice, which is better observed with neutrons. This gives the Bragg peaks in the neutron scattering patterns a broadened appearance as the diffuse scattering increases and overlaps the bases of the Bragg peaks. Simple analysis of the diffuse scattering was performed through manipulation of the background polynomial used in Rietveld refinements by monitoring the quality of the fits (Table 4). The background polynomial of the $Ho_2Ti_2O_7$ endmember was applied to the patterns of the other members to include the diffuse scattering in the refinements.
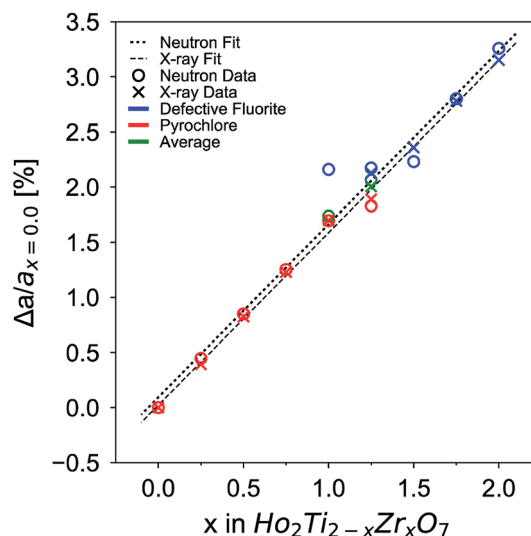

Fig. 3 Change of unit cell parameter with respect to that of the titanate endmember ($x = 0$), $\Delta a/a_{x=0}$ ($a = a_P$ and $2a_{DF}$), as a function of increasing Zr-content, x. Data points from neutron and X-ray data are given by circles and crosses, respectively. Data points corresponding to the pyrochlore phase are given in red, defect fluorite in blue, and average parameters of the two-phase compositions in green. Error bars are smaller than the symbols. The dotted line is a linear fit to neutron data and the dashed line to X-ray data. The goodness of fit values, R^2, for each fit are above 0.995.

All members that were refined primarily with the pyrochlore structure ($x = 0.25–1.0$) exhibited small decreases in fit quality (<0.3% increase in R_w). Compositions refined primarily with the defect fluorite structure ($x = 1.25–2.0$) whose structure functions had distinct diffuse scattering peaks exhibited the greatest decrease in fit quality (2–4% increase in R_w). A more detailed understanding of the origin of the diffuse scattering is obtained with Fourier analysis of the structure functions in the form of PDFs.

3.2 Short-range structure – neutron and X-ray real space (PDF) analysis

Neutron and X-ray PDFs are an intuitive, real-space representation of the atomic configuration and were used to gain further insight into the nature of disorder across the solid solution series over the short- and intermediate-range length scales (Fig. 4). Peak positions in the PDFs give information on interatomic distances, peak areas on coordination numbers, and peak widths on the atomic thermal vibrations and accumulated

disorder. Single peaks can contain information on multiple atomic pairs, such as the negative peak at 1.95 Å in the neutron PDF of $Ho_2Ti_2O_7$ which gives information on the nearest neighbor Ti–O octahedral correlations (Fig. 4a). Increasing disorder is apparent in the PDFs across all r-space as several distinct, sharp peaks merge into fewer broad peaks with increasing Zr-content, x. For example, multiple peaks associated with various atomic correlations in the region from 9.0 to 10.5 Å merge together with increasing x (Fig. 4a and b). Peak intensities increase across r-space due to the negatively scattering Ti being replaced by the positively scattering Zr (Table 1). Furthermore, peaks at higher r-space are broader and less numerous than at lower r-space due to very large atomic shells with many atoms that average together. The long-range PDFs (r > 25 Å, not shown) of compositions with higher x values indicate more disorder than the short-range PDFs, indicating there is some degree of local order associated with these compositions.

Analysis of the nearest neighbor cation–anion correlations at low r-space in the neutron PDFs (1.7 to 3.5 Å) (Fig. 4c) that form the coordination polyhedra give direct insight into the local
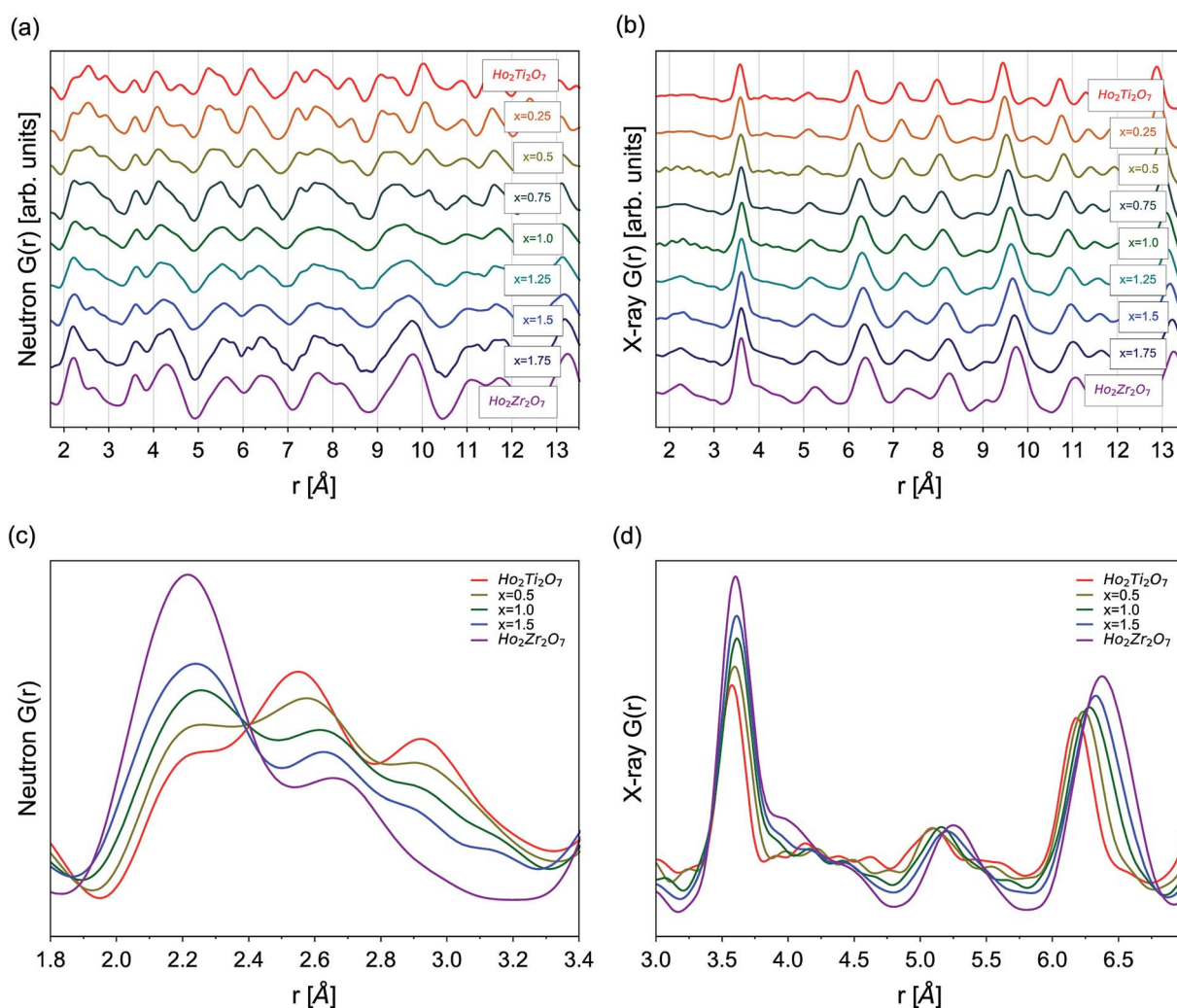

Fig. 4 (a) Neutron and (b) X-ray PDFs, $G(r)$, from 1.7 to 13.5 Å for $Ho_2Ti_{2−x}Zr_xO_7$ series. Overlay of selected series members' (x = 0.0, 0.5, 1.0, 1.5, 2.0) (c) neutron PDFs at low-r from 1.8 Å to 3.4 Å and (d) X-ray PDFs from 3.0 to 7.0 Å.

atomic configuration. The negative scattering length of Ti leads to a negative partial PDF, $g_{Ti-X}(r)$, highlighting atomic correlations that are only associated with Ti–X (X = Ho, Zr, O) distances. When Ti is replaced by Zr its negative scattering contribution is reduced, decreasing the intensity of the negative Ti–O peak at 1.95 Å. As the Zr-content increases, Zr not only replaces Ti but also occupies sites regularly filled by Ho, seen in the PDFs as the broadening and intensifying of the peak at 2.2 Å, which contains many of the nearest neighbor cation–oxygen bond correlations. The O–O peaks at 2.6 Å and 2.95 Å broaden and reduce in intensity with increasing x due to the O–O bonds adopting a more varied distribution of lengths. The cation–cation correlations at slightly higher r-space are best analyzed in the X-ray PDFs (1.7 to 7.0 Å) that are highly sensitive to cation position (Fig. 4d). The first few peaks from 1.7 Å to 3.2 Å have extremely low intensities due to the weak cation–anion and anion–anion correlations. Only a general increase of intensity of these peaks with increasing Zr-content, x, can be observed with no discernable shape changes. Truncation ripples are present in the $x = 0.5$ and 1.0 samples, likely due to experimental differences such as reduced packing fraction of these powders. The first prominent peak at 3.57 Å contains all nearest-neighbor cation–cation correlations and the peak intensity gradually increases as Zr replaces Ti. A broad shoulder at ~4.0 Å indicates that the incorporation of Zr lengthens a portion of these distances significantly beyond what would be observed for different cation sites. Peaks at higher r-values exhibit significant broadening with increasing disorder and little shape change, such as the development of new peaks and shoulders or peak merging. This is not the case in the neutron PDFs where the peaks are constantly changing shape with increasing Zr-content across the entire r-range, which indicates that the oxygen sublattice is subject to more changes than the cation sublattice as Ti is replaced with Zr and disorder accumulates.

The long-range structural models determined using Rietveld refinement for each composition were applied to the PDF *via* small-box refinement from $r = 1.7$ to 50 Å (Table 4). This resulted in, except for the $Ho_2Ti_2O_7$ endmember, poor fits for all compositions ($R_{wp} > 25\%$), especially at low r-values where local distortions exist. "Boxcar" refinements were used to determine the spatial range of the local deviations in the long-range structure (Fig. 5). The exclusion of the PDF region that contains the coordination polyhedra bond correlations (solid line) significantly improved the goodness-of-fit values of small-box refinements beyond the dimensions of the $Fd\bar{3}m$ ordered pyrochlore unit cell (long dashed line) and larger. The PDFs of the compositions whose diffraction patterns were consistent with the ordered pyrochlore structure (circles) were in general better modelled at low r_{min} values than those that exhibit the $Fm\bar{3}m$ disordered, defect fluorite long-range structure (crosses). The goodness-of-fit values at all r_{min} values tend to worsen with increasing Zr-content, with the exception of the $Ho_2Zr_2O_7$ endmember which exhibits high R_{wp} values at low r_{min} that fall to similar values as the $Ho_2Ti_2O_7$ endmember beyond dimensions of the defect fluorite unit cell (short dashed line). Additionally, the two endmembers' R_{wp} values were lower as

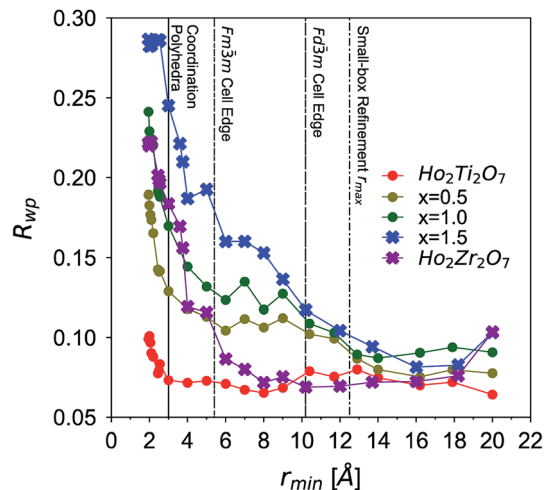Fig. 5 Goodness-of-fit parameters (R_{wp}) of $Ho_2Ti_{2-x}Zr_xO_7$ compositions ($x = 0.0$, 0.5, 1.0, 1.5, and 2.0) over various r-ranges based on "boxcar" refinements of neutron PDFs using corresponding long-range structural models. The x-axis represents the minimum r-value of each 10 Å fit window (*e.g.*, 1.7–11.7 Å) used in the refinement procedure. Boxcar refinements with the $Fd\bar{3}m$ pyrochlore model are represented by circles and those with the $Fm\bar{3}m$ defect fluorite model by crosses. Lines are drawn to guide the eye. A higher R_{wp} value means a worse quality fit. Vertical lines in background represent approximate upper r-range limits of nearest neighbor coordination polyhedra bond lengths (solid line, <3.0 Å), defect fluorite cell edge (short dashed line, <5.2 Å), pyrochlore cell edge (long dashed line, <10.1 Å), and r_{max} used for small-box refinements (dotted dashed line, <12.5 Å).
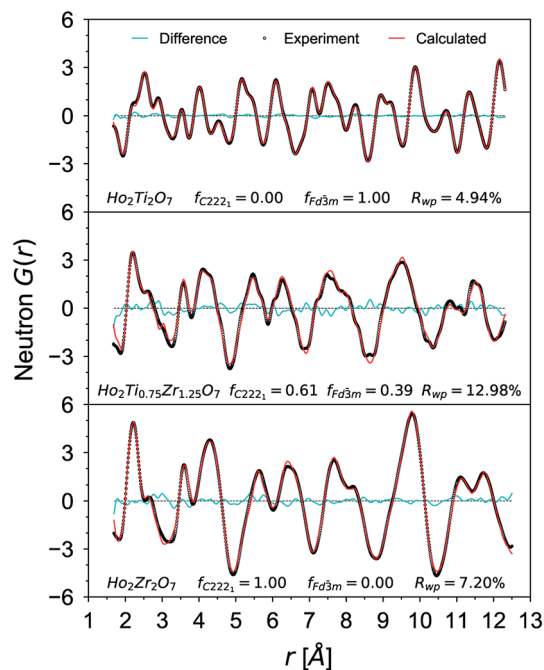

Fig. 6 Neutron PDF data (black circles) of $Ho_2Ti_2O_7$, $Ho_2Ti_{0.75}Zr_{1.25}O_7$, and $Ho_2Zr_2O_7$ with small-box refinements (red curves) using the $Fd\bar{3}m$, mixed $Fd\bar{3}m/C222_1$, and $C222_1$ phase models, respectively. The difference curves between model and data are given as cyan lines and f_{C222_1} and $f_{Fd\bar{3}m}$ denotes for the weberite-type and pyrochlore phase fractions.

compared to the intermediate series members that share the same long-range phase.

Small-box refinements were performed on the neutron and X-ray PDFs with refinement limits that were established from the "boxcar" analysis ($r = 1.7$–12.5 Å, Fig. 5 dotted dashed line). Only the PDF for the $Ho_2Ti_2O_7$ endmember was fully refined using solely the pyrochlore $Fd\bar{3}m$ space group (Fig. 6). The intermediate compositions that are well-modelled over the long-range with the pyrochlore structure ($x = 0.25$ to 0.75) deviate from the ordered pyrochlore structure over short length scales ($r < 12.5$ Å). In contrast, all PDFs associated with sample compositions that are best refined on the long-range with the defect fluorite structure ($x = 1.5$ to 2.0) cannot be modelled locally with the $Fm\bar{3}m$ space group. Furthermore, the two members that exhibit two phases on the long-range ($x = 1.0$ and 1.25) cannot be locally refined using the pyrochlore/defect fluorite two-phase model. The PDF of the fully disordered $Ho_2Zr_2O_7$ endmember is best refined using a weberite-type structural model.[41] Among the many forms of weberite-type ordering,[84] the best fit in this study was obtained with a model isostructural with Y_3TaO_7 ($C222_1$). This model is described in depth elsewhere.[45,46] This structure is very similar to $Ccmm$ and has been previously used to describe the local atomic arrangement in A_3BO_7 defect fluorite materials.[43] The 16h oxygen site is split into two 8c sites and most cations and anions in the structure have more positional and vibrational degrees of freedom than in $Ccmm$. The unit cell parameters used for both the $Fd\bar{3}m$ and $C222_1$ structural models are reported in Table 1. Although the $C222_1$ space group has more degrees of structural freedom than $Fd\bar{3}m$, the two cations and the anion vacancy are more ordered than in $Fm\bar{3}m$. Similar to the results by Shamblin *et al.*, this weberite-type model fits the PDF of the $Ho_2Zr_2O_7$ endmember very well out to an r-value of 12.5 Å, beyond which the PDF is best fit by the long-range $Fm\bar{3}m$ model.[42]

The details of the two-phase model and site occupancies were constructed based on the neutron PDF data by assigning the Ti sites to the $Fd\bar{3}m$ phase and the Zr sites to $C222_1$. This configuration provided the best fit results and other model permutations resulted in poor fits with large average R_{wp} values, unphysical coordination polyhedra geometries, and non-stoichiometric compositions (Table 5). Permutations where Ti was forced into a weberite-type configuration resulted in the least agreement between model and data, followed by permutations where Zr was forced into a pyrochlore arrangement. Refinement of both the neutron and X-ray PDFs of the fully disordered $Ho_2Zr_2O_7$ endmember with the $C222_1$ model yielded a fit of poorer quality than the ordered pyrochlore $Ho_2Ti_2O_7$ endmember which was refined with the $Fd\bar{3}m$ model (Table 6). All intermediate compositions of the solid-solution series were best described by a "two-phase" $Fd\bar{3}m/C222_1$ model as shown in Fig. 6 representative for the $x = 1.25$ composition. The $C222_1$ phase fraction systematically increased with Zr-content over the compositional range. The same two-phase model was applied to neutron and X-ray data but the R_{wp} values of the X-ray PDF fits were consistently lower for all intermediate compositions. Since X-rays are more sensitive to the cation positions, the trend in

Table 5 Neutron PDF model permutation study results

Structural configuration	$\overline{R_{wp}}^a$ (%)	Outcome of results
Ti $\Rightarrow Fd\bar{3}m$ Zr $\Rightarrow C222_1$	10.31	Model used for this study
Ti $\Rightarrow Fd\bar{3}m$ Zr $\Rightarrow Fd\bar{3}m$	14.89	Nonphysical structure
Ti $\Rightarrow C222_1$ Zr $\Rightarrow C222_1$	21.57	Non-stoichiometric
Ti $\Rightarrow C222_1$ Zr $\Rightarrow Fd\bar{3}m$	—	Failure to converge

[a] Average of R_{wp} values for refinements of all compositions.

Table 6 Refined parameter values and errors for PDF refinements

Neutron total scattering (fit range $r = 1.7$–12.5 Å)

Composition	Structure	$C222_1$ fraction, y	R_{wp} (%)
$Ho_2Ti_2O_7$	$Fd\bar{3}m$	0	4.94
$Ho_2Ti_{1.75}Zr_{0.25}O_7$	$Fd\bar{3}m + C222_1$	0.14(2)	9.01
$Ho_2Ti_{1.50}Zr_{0.50}O_7$	$Fd\bar{3}m + C222_1$	0.23(2)	9.16
$Ho_2Ti_{1.25}Zr_{0.75}O_7$	$Fd\bar{3}m + C222_1$	0.35(2)	12.91
$Ho_2Ti_{1.00}Zr_{1.00}O_7$	$Fd\bar{3}m + C222_1$	0.45(4)	10.48
$Ho_2Ti_{0.75}Zr_{1.25}O_7$	$Fd\bar{3}m + C222_1$	0.61(2)	12.98
$Ho_2Ti_{0.50}Zr_{1.50}O_7$	$Fd\bar{3}m + C222_1$	0.69(5)	11.58
$Ho_2Ti_{0.25}Zr_{1.75}O_7$	$Fd\bar{3}m + C222_1$	0.87(1)	13.04
$Ho_2Zr_2O_7$	$C222_1$	1	7.20

X-ray total scattering (fit range $r = 3.2$–12.5 Å)

Composition	Structure	$C222_1$ fraction, y	R_{wp} (%)
$Ho_2Ti_2O_7$	$Fd\bar{3}m$	0	6.89
$Ho_2Ti_{1.75}Zr_{0.25}O_7$	$Fd\bar{3}m + C222_1$	0.13(3)	5.29
$Ho_2Ti_{1.50}Zr_{0.50}O_7$	$Fd\bar{3}m + C222_1$	0.22(3)	4.93
$Ho_2Ti_{1.25}Zr_{0.75}O_7$	$Fd\bar{3}m + C222_1$	0.34(2)	4.59
$Ho_2Ti_{1.00}Zr_{1.00}O_7$	$Fd\bar{3}m + C222_1$	0.46(2)	5.69
$Ho_2Ti_{0.75}Zr_{1.25}O_7$	$Fd\bar{3}m + C222_1$	0.59(2)	6.40
$Ho_2Ti_{0.50}Zr_{1.50}O_7$	$Fd\bar{3}m + C222_1$	0.70(2)	7.37
$Ho_2Ti_{0.25}Zr_{1.75}O_7$	$Fd\bar{3}m + C222_1$	0.86(2)	8.29
$Ho_2Zr_2O_7$	$C222_1$	1	8.82

the goodness-of-fit values indicates that the cationic arrangement, with Zr and Ho occupying the 7-coordinated sites and Ti remaining in the 6-coordinated sites, is a good model for the cation sublattice. Conversely, X-rays have poor sensitivity to the anion sublattice and thus the neutron fits are necessary to completely evaluate the effectiveness of the two-phase model. The increase in the R_{wp} values of the neutron PDF fits with increasing Zr-content shows that the disorder present is more complex than can be fully captured by this model.

3.3 Enthalpy of formation and mixing – high temperature oxide melt solution calorimetry

After non-destructive neutron and X-ray characterization, all $Ho_2Ti_{2-x}Zr_xO_7$ sample compositions were analyzed using high

temperature solution calorimetry. Fig. 7a shows the measured enthalpies of drop solution, ΔH_{ds}, *versus* Zr-content, x. These values are summarized in Table 7. The enthalpy of drop solution is the highest for the fully ordered $Ho_2Ti_2O_7$ endmember with a value of 126.0 ± 0.5 kJ mol^{-1} and systematically decreases with increasing x to -16.4 ± 0.8 kJ mol^{-1} for the fully disordered $Ho_2Zr_2O_7$ endmember. The dissolution behavior of the series is decreasingly endothermic with $Ho_2Zr_2O_7$ being the only member that dissolves exothermically. The trend in ΔH_{ds} deviates from an ideal linear behavior and is best described as a function of increasing mole fraction of $Ho_2Zr_2O_7$ ($x/2$) with a second-degree polynomial equation:
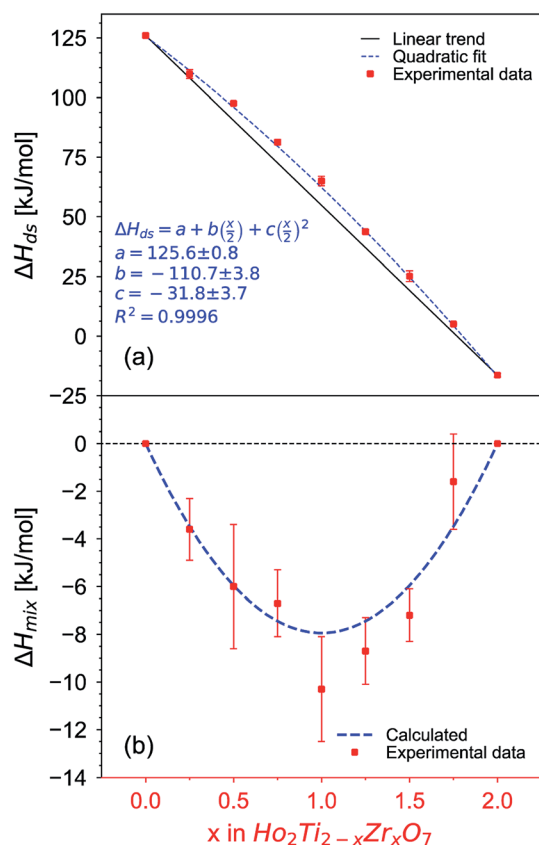
$$\Delta H_{ds} = a + b\left(\frac{x}{2}\right) + c\left(\frac{x}{2}\right)^2 \qquad (6)$$

with fit parameters $a = 125.6 \pm 0.8$, $b = -110.7 \pm 3.8$, and $c = -31.8 \pm 3.7$ kJ mol^{-1}. The quadratic form is equivalent to a regular solid solution formalism[85–87] with c in eqn (6) being

Table 7 Enthalpies of drop solution (ΔH_{ds}) in $3Na_2O \cdot 4MoO_3$ solvent at 800 °C and enthalpies of formation from oxides ($\Delta H_{f,ox}^{\circ}$) in the solid solution series $Ho_2Ti_{2-x}Zr_xO_7$ ($0 \leq x \leq 2.00$)[a]

x in $Ho_2Ti_{2-x}Zr_xO_7$	ΔH_{ds} (kJ mol^{-1})	$\Delta H_{f,ox}^{\circ}$ (kJ mol^{-1})
0	$126.0^8 \pm 0.5$	-88.7 ± 2.0
0.25	$109.8^8 \pm 1.8$	-83.6 ± 2.7
0.50	$97.6^6 \pm 0.6$	-82.4 ± 2.2
0.75	$81.3^8 \pm 1.1$	-77.2 ± 2.5
1.00	$65.0^8 \pm 2.0$	-72.0 ± 2.7
1.25	$43.7^7 \pm 1.0$	-61.7 ± 3.0
1.50	$25.2^4 \pm 2.3$	-54.3 ± 3.9
1.75	$5.1^4 \pm 0.3$	-45.2 ± 3.4
2.00	$-16.4^7 \pm 0.8$	-34.8 ± 3.8

[a] 4,6,7,8 number of drops.

Fig. 7 (a) Enthalpy of drop solution, ΔH_{ds}, as a function of Zr-content, x, in $Ho_2Ti_{2-x}Zr_xO_7$ (Table 7). Error bars are smaller than the symbol for some compositions. The blue dashed curve is a fit to the data points using a second-degree polynomial function (eqn (6) with fit values given) and the black solid line represents ideal linear behavior between the two endmembers. (b) Corresponding enthalpies of mixing, ΔH_{mix}, determined using eqn (7) (red data points) and ΔH_{mix} calculated from the quadratic fit to ΔH_{ds} (blue dashed curve) (Table 8) using the formula ΔH_{mix} (calc.) = $W \times (x/2) \times (1 - x/2)$, where W = interaction parameter and $x/2$ = mole fraction of $Ho_2Zr_2O_7$. Uncertainties of ΔH_{mix} are propagated ΔH_{ds} errors.

analogous to the interaction parameter, W. An interaction parameter of zero indicates ideal mixing with the only difference in thermodynamic properties arising from the mixing of different atoms on structurally equivalent sites (configurational entropy). A negative interaction parameter (exothermic mixing) suggests more favorable interactions between unlike species than between like species and indicates a tendency for short-range ordering of these species. Negative interaction parameters have been also observed in the fluorite related ZrO_2–RE_2O_3, HfO_2–RE_2O_3, CeO_2–RE_2O_3 binary oxide solid solution series with RE being a rare earth cation.[52–57]

From the measured ΔH_{ds} the enthalpies of mixing (formation of solid solutions from the two endmembers), ΔH_{mix}, as a function of x were determined using the following equation:

$$\Delta H_{mix} = -\Delta H_{ds}[Ho_2Ti_{2-x}Zr_xO_7] + \left(\frac{x}{2}\right)\Delta H_{ds}[Ho_2Zr_2O_7]$$
$$+ \left(1 - \frac{x}{2}\right)\Delta H_{ds}[Ho_2Ti_2O_7] \qquad (7)$$

The enthalpies of mixing decrease with increasing Zr-content x to a minimum at -10.3 ± 2.2 kJ mol^{-1} for the intermediate composition $x = 1.0$ and then increase again with further substitution of Ti by Zr (Fig. 7b and Table 8). The trend of ΔH_{mix} is very similar in shape and magnitude to those reported for the aforementioned binary oxide solid solutions.[50–55] This behavior was attributed to the formation of ordered nanoscale clusters involving cations, oxygen, and oxygen vacancies.[52–57] A fit of the ΔH_{mix} data was produced by calculating ΔH_{mix} values from the quadratic fit of ΔH_{ds} using eqn (7). This results in a smooth parabola that better predicts the magnitude of the minimum at $x = 1.0$, which is -7.9 kJ mol^{-1} (Table 8). The endmembers' structures have different symmetries but are related as they are both derived from fluorite, with the ordered structure being a subgroup of the disordered defect fluorite structure. Thus, the accumulation of disorder may be gradual, and the observed phase transition could be second order. The enthalpy of mixing in the $Ho_2Ti_2O_7$–$Ho_2Zr_2O_7$ solid solution series portrays no anomaly near the order–disorder transition point where the symmetry changes and we consider

Table 8 Enthalpies of mixing of $Ho_2Ti_{2-x}Zr_xO_7$ ($0 \leq x \leq 2.00$) solid solution considering mole fraction of $Ho_2Zr_2O_7$ ($x/2$) and phase fraction of weberite-type (y)

x in $Ho_2Ti_{2-x}Zr_xO_7$	$\Delta H_{mix}{}^a$ (kJ mol^{-1})	Calculated $\Delta H_{mix}{}^c$ (kJ mol^{-1})	Phase fraction of weberite-type, y	$\Delta H_{mix}{}^b$ (kJ mol^{-1})	Calculated $\Delta H_{mix}{}^c$ (kJ mol^{-1})
0	0	0	0	0	0
0.25	-3.6 ± 1.3	-3.5	0.14(2)	-3.2 ± 1.7	-1.9
0.50	-6.0 ± 2.6	-6.0	0.23(2)	-4.3 ± 1.0	-2.8
0.75	-6.7 ± 1.4	-7.4	0.35(2)	-4.7 ± 1.4	-3.6
1.00	-10.3 ± 2.2	-7.9	0.45(4)	-5.1 ± 1.4	-3.9
1.25	-8.7 ± 1.4	-7.4	0.61(2)	-4.5 ± 1.2	-3.8
1.50	-7.2 ± 1.1	-6.0	0.69(5)	-3.0 ± 1.6	-3.4
1.75	-1.6 ± 2.0	-3.5	0.87(7)	-2.4 ± 1.4	-1.8
2.00	0	0	1	0	0

^{a} ΔH_{mix} (kJ mol^{-1}) (experimental) considering mole fraction of $Ho_2Zr_2O_7$ ($x/2$) obtained using eqn 7. ^{b} ΔH_{mix} (kJ mol^{-1}) (experimental) considering phase fraction of weberite-type (y) obtained using $\Delta H_{mix} = -\Delta H_{ds}[Ho_2Ti_{2-x}Zr_xO_7] + y\Delta H_{ds}[Ho_2Zr_2O_7] + (1 - y)\Delta H_{ds}[Ho_2Ti_2O_7]$. ^{c} Calculated from values of the second-degree fits of the ΔH_{ds} data using eqn 7.

the system to form a continuous solid solution with a gradually increasing degree of disorder. The negative heat of mixing fit by a regular solution parameter is consistent with this behavior and with some amount of short-range ordering.
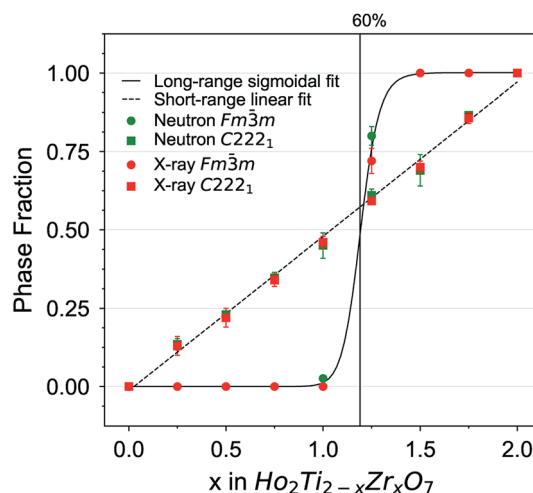
The enthalpies of formation from binary oxides, $\Delta H_{f,ox}^\circ$, for the $Ho_2Ti_{2-x}Zr_xO_7$ system are all exothermic (Table 7), suggesting enhanced stability relative to the binary oxides, but they become less exothermic with increasing Zr-content, ranging from -88.7 ± 2.0 kJ mol^{-1} for the ordered $Ho_2Ti_2O_7$ endmember to -34.8 ± 3.8 kJ mol^{-1} for the disordered $Ho_2Zr_2O_7$ endmember (Table 7).

4. Discussion

4.1 Structural data

Combined neutron and X-ray total scattering provide unique insight into the pyrochlore-to-defect fluorite disordering process and how it proceeds at the long- and short-range scales across the $Ho_2Ti_{2-x}Zr_xO_7$ solid solution series through comparison of the Rietveld and small-box refinements. While previous investigations have addressed this order–disorder transition with different local and long-range analytical probes, total scattering experiments with PDF analysis allow simultaneous study, and thus direct comparison, of the atomic structure at different length scales. The $C222_1$ weberite-type phase fraction (determined through PDF analysis) is a measure for the short-range disorder, while the long-range $Fm\bar{3}m$ defect fluorite phase fraction, the pyrochlore 8a oxygen occupancy n_{8a}, and the pyrochlore 48f oxygen x-position x_{48f} (determined through Rietveld refinement) are measures of the long-range disorder. The transition from the fully ordered pyrochlore structure ($Ho_2Ti_2O_7$) to the fully disordered, defect fluorite structure ($Ho_2Zr_2O_7$) is complex and has a distinct dependence on the Zr-content, x, across different length scales (Fig. 8). The long-range structure exhibits a fairly abrupt change in ordering, with the defect fluorite phase fraction following sigmoidal behavior. The diffraction patterns of almost all samples were fully refined with either the $Fd\bar{3}m$ (Ti-rich compositions) or the $Fm\bar{3}m$ (Zr-rich

compositions) phase, and only the intermediate compositions $x = 1.0$ and 1.25 exhibited coexistence of both phases. With increasing Zr-content, the ordered pyrochlore phase persists until more than 50% of Ti is replaced by Zr which then triggers over the long-range a nearly complete disordering to defect fluorite across a narrow compositional range centered around $x \approx 1.2$ (Fig. 8). The oxygen site parameters (x_{48f} and n_{8a}), which indicate the degree of disorder of the anion sublattice, increase in a similar manner to the defect fluorite phase fraction (not shown). This would suggest that both the cation and anion sublattices disorder together over the same compositional regimes. This behavior is in agreement with previous studies on the $Y_2Ti_{2-x}Zr_xO_7$ and $Ho_2Ti_{2-x}Zr_xO_7$ systems which show

Fig. 8 Quantitative analysis of disorder from neutron and X-ray total scattering data in the $Ho_2Ti_{2-x}Zr_xO_7$ series. Phase fractions of long-range defect fluorite ($Fm\bar{3}m$) and short-range weberite-type ($C222_1$) are plotted as a function of Zr-content, x. Error bars from phase analysis are for several data points smaller than the symbols. A symmetric sigmoid function (solid) and a straight line (dashed) were fitted to the defect fluorite and weberite-type data points, respectively, with a goodness of fit value R^2 of more than 0.998.

Paper

a similar abrupt transition from pyrochlore to defect fluorite with the two phases coexisting around $x \approx 1.2$.[31,36] In the present solid solution series, the more step-like order–disorder transition across the long-range is in clear contrast to the more gradual accumulation of disorder at the local scale. The weberite-type phase fraction increases linearly at the expense of the pyrochlore phase (Fig. 8) and apart from the two end-members, both phases coexist locally for all compositions measured. Such a gradual increase in short-range modifications has been observed in previous studies on $Y_2B_{2-x}Zr_xO_7$ (B = Ti or Sn) pyrochlore using Raman spectroscopy, magic angle spinning nuclear magnetic resonance (MAS NMR), and X-ray absorption near-edge structure (XANES).[38,39] While it has been shown before that fully ordered compositions are pyrochlore on both the long- and short-range and that fully disordered compositions are defect fluorite on the long-range and weberite-type on the short-range,[42] this study reveals a complex behavior for intermediate compositions. The degree of disorder is, for a given composition, distinct at different length scales and the evolution of the structure on the long- and short-range with changes in composition appears to be decoupled. Compositions which are ordered over the long-range (*e.g.*, $x = 0.75$ with 37.5% Zr) still locally contain a large fraction of the weberite-type phase (~35%).

The immediate formation of a local weberite-type phase in $Ho_2Ti_2O_7$ pyrochlore upon the substitution of any amount of Zr can be understood by a detailed comparison of the two structures. Observation of pyrochlore along the [110] direction reveals repeating layers of distinct 6- and 8-fold sites (Fig. 1a). This is similar to the weberite-type structure which also contains 6- and 8-fold site layers but with intermediate layers of 7-fold sites occupied by a random mix of Ho and Zr cations and an ordered arrangement of oxygen anion defects (Fig. 1c). Indeed, Zr is coordinated by seven oxygen anions in monoclinic zirconia[88,89] and has been previously observed to adopt a 7-coordinated environment within the pyrochlore matrix.[25,31,35] Recent work using Pauling's rules has proposed that the formation of 7-coordinated sites is driven by either the direct movement of 48f oxygen anions into 8a sites, or through an indirect path where the 8b oxygen anions migrate into 8a sites and then are immediately occupied by 48f oxygen anions.[46] Both atomic-scale movements explain the retention of oxygen in the 8b site deduced using Rietveld refinement. This movement creates a short-range polyhedral arrangement that is nearly indistinguishable from the weberite model in A_3BO_7 oxides and provides a coordination environment that is better suited to accommodate the larger Zr cations. First-principles calculations support this theory and show the lowest energy structures are attained by oxygen relaxations that allow for 7-coordinated Zr cations.[90] O'Quinn *et al.* show these short-range polyhedral arrangements (essentially weberite-type nanodomains) form in the pyrochlore matrix such that the configurational average of all potential orientations yields the long-range defect fluorite structure.[46] This behavior can also be understood based on a weberite-type building block model. Movement of an oxygen anion forms a weberite-type building block within the pyrochlore matrix, but limits the motion of other nearby oxygen

anions, establishing a minimum distance between weberite-type building blocks. This is a direct result of applying Pauling's rules, which dictates that the other oxygen anions associated with this building block must remain with this 7-coordinated Zr cation.[46] A direct comparison of the short- and long-range behavior in the present solid solution series reveals that weberite-type building blocks will gradually form until a critical density is reached (50% of Ti replaced by Zr) which triggers the long-range transformation to an average defect fluorite (Fig. 8). A similar behavior has been previously observed in ion-irradiated sesquioxides (A_2O_3) in which oxygen defects are formed under irradiation far from each other and trigger a phase transformation (cubic-to-monoclinic) upon reaching a critical density.[91]

The diffuse scattering observed in the neutron structure functions, $S(Q)$, of the $Ho_2Ti_{2-x}Zr_xO_7$ series (Fig. 2) gives further insight on how the local structural arrangements translate to the long-range structure. Individual weberite-type building blocks formed from a single oxygen defect within the pyrochlore matrix are on the order of a nanometer as shown by the boxcar refinement (Fig. 5). The diffuse scattering is likely produced by the correlated differences between randomly oriented larger weberite-type nanodomains and the average crystal matrix. An approach developed by Neder *et al.*[74] was used to model coherent weberite-type and pyrochlore nanodomains to replicate diffuse scattering in the neutron total scattering data of the $x = 1.75$ composition with an average defect fluorite structure (Fig. 9). This composition was chosen as its $S(Q)$ shows distinct
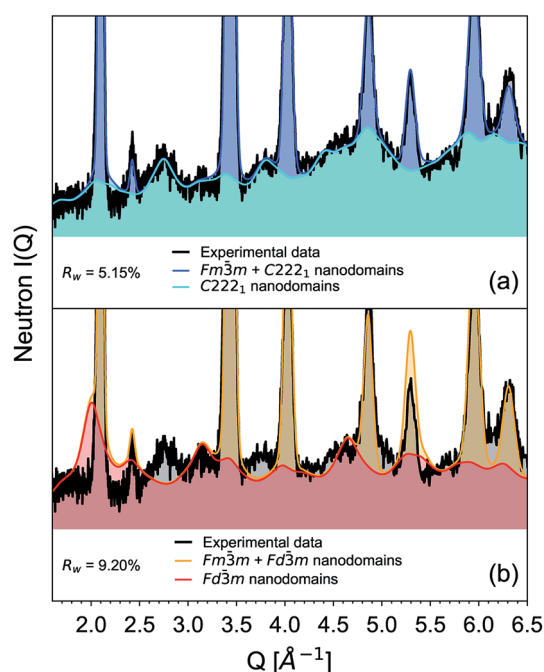

Fig. 9 Diffuse scattering analysis using neutron scattering data (black) and Rietveld refinement using the approach by Neder *et al.*[74] (a) Defect fluorite ($Fm\bar{3}m$, blue) plus weberite-type nanodomains ($C222_1$, cyan) refinement. (b) Defect fluorite ($Fm\bar{3}m$, orange) plus pyrochlore nanodomains ($Fd\bar{3}m$, red). Key features not fit are marked with a diamond. The coherent nanodomains were modelled to be 4 nm.

diffuse scattering with several prominent peak-like features. The integral diffracted intensity was split into the long-range average structure (Bragg peaks) and a "difference" structure (diffuse scattering, *i.e.*, nanodomains). The model using weberite-type ($C222_1$) nanodomains in a defect fluorite $Fm\bar{3}m$ matrix (Fig. 9a) replicated both the diffuse scattering peaks and the Bragg peaks well ($R_w = 5.15\%$). The model using a pyrochlore ($Fd\bar{3}m$) nanodomain model (Fig. 9b) replicated diffuse features at $Q = 3.2$ and 4.7 Å^{-1}, but captured less of the diffuse scattering ($Q = 2.7, 3.7, 4.5–5.1$ Å^{-1}), over and under fit several Bragg peaks ($Q = 2.1$ and 5.3 Å^{-1}), and in general produced a lower quality fit ($R_w = 9.20\%$). This behavior reflects the short-range structure obtained for this composition using PDF small-box modeling, showing a predominantly weberite-type atomic arrangement with the retention of some character of pyrochlore ordering. These goodness-of-fit values (R_w) should not be directly compared to those of the standard Rietveld refinement results as difference modelling uses significantly more parameters. The nanodomain modeling shows that while weberite-type and pyrochlore building blocks are responsible for the short-range structure in the PDF, larger nanodomains of both phases are responsible for the diffuse scattering observed at high Zr-content. Therefore, this diffuse scattering represents the intermediate-range structure which is important in understanding the formation of the long-range defect fluorite. Further work using advanced reverse Monte Carlo (RMC) and molecular dynamics (MD) modelling may help elucidate these processes and describe the structural heterogeneity in disordered pyrochlore oxides.

4.2 Thermodynamic data

The thermodynamic data provide further insight into the role of local atomic arrangements associated with the disordering process across the Ho$_2$Ti$_{2-x}$Zr$_x$O$_7$ solid solution series. Several factors contribute to ΔH_{ds} and ΔH_{mix} in binary and pseudobinary solid solutions, four of which were considered by Davies and Navrotsky:[92] (i) size difference, (ii) valence of cations being mixed, (iii) electronic configuration, and (iv) covalency difference. The first two factors are most significant for the Ho$_2$Ti$_{2-x}$Zr$_x$O$_7$ system and hinder cationic mixing as Ti^{4+} and Zr^{4+} have different ionic sizes (Table 2) and high valences. Since the electronic configuration of Ti^{4+} and Zr^{4+} and the ionic character of the M–O bond for each cation are similar, these terms are considered less important. Following the approach developed by Davies and Navrotsky,[92] one obtains a positive interaction parameter of +25 kJ mol^{-1} for ΔH_{ds} resulting from the size difference of the two cations being fully mixed (Zr^{4+} and Ti^{4+}). The experimentally determined interaction parameter of -32 kJ mol^{-1} (eqn (6)) suggests that disordering in this solid solution series can be associated to a value of -57 kJ mol^{-1} (-57 kJ mol^{-1} + 25 kJ mol^{-1} = -32 kJ mol^{-1}) which is quite exothermic, indicating these rearrangements are highly favorable. Such a strongly exothermic interaction parameter weakens the strict applicability of a regular solution approach because the large extent of short-range order will diminish the entropy of mixing significantly from that of a random distribution of

cations, anions, and vacancies. Thus, the interaction parameter for Ho$_2$Ti$_{2-x}$Zr$_x$O$_7$ should be considered more as a convenient fitting parameter than as a stringent physical description of the system. For a full thermodynamic description, more complex mixing models are required.

Realizing the importance of the weberite-type domains in the disordering process, ΔH_{ds} was plotted against the fraction of the local weberite-type phase, y, determined from structural analysis (Fig. 10a). The new ΔH_{ds} data is also fit by a second-degree polynomial equation:

$$\Delta H_{ds} = a' + b'y + c'y^2 \tag{8}$$

with fit parameters $a' = 126.5 \pm 1.6$, $b' = -129.5 \pm 8.8$, and $c' = -12.8 \pm 8.6$ kJ mol^{-1}. In contrast to the behavior shown in Fig. 7a, the enthalpies of drop solution deviate only slightly
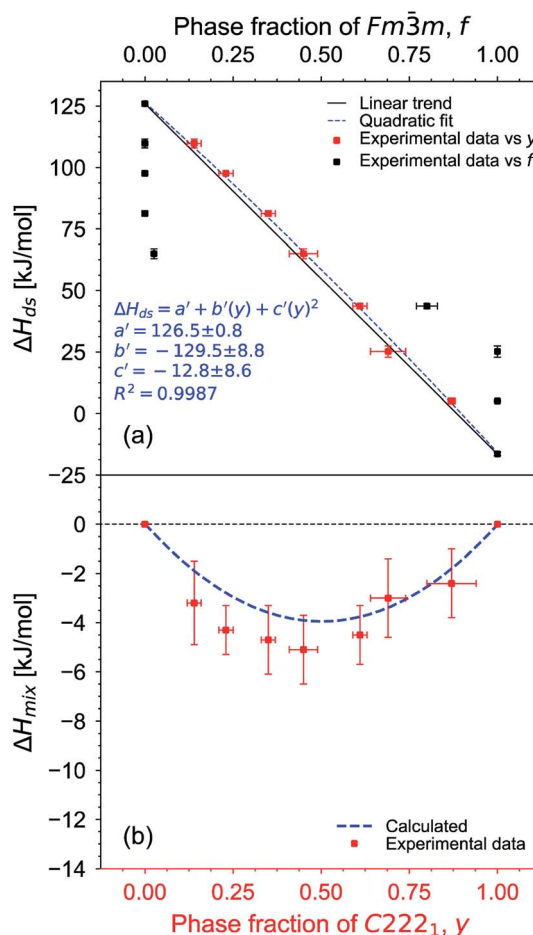

Fig. 10 (a) Enthalpy of drop solution, ΔH_{ds}, of Ho$_2$Ti$_{2-x}$Zr$_x$O$_7$ as a function of phase fraction of weberite-type $C222_1$, y (red), and defect fluorite $Fm\bar{3}m$, f (black). Error bars are smaller than the symbol for some compositions. The blue dashed curve is a fit to the data points *versus* y using a second-degree polynomial function (eqn (8) with fit values given) and the black solid line represents ideal linear behavior based on the two endmembers. (b) Corresponding enthalpies of mixing, ΔH_{mix}, determined using eqn (7) (red data points) and ΔH_{mix} calculated from the quadratic fit to ΔH_{ds} *versus* y (blue dashed curve) (Table 8). Uncertainties of ΔH_{mix} are propagated ΔH_{ds} errors. Fig. 10 plotted on the same scale as Fig. 7 for direct comparison.

from a straight line and the interaction parameter c' may be zero within experimental error if one considers also uncertainties in weberite-type phase fraction and other possible sources of error. The corresponding enthalpies of mixing, ΔH_{mix}, determined using eqn (7) by replacing mole fraction ($x/2$) with weberite phase fraction (y), exhibits parabolic behavior with y reaching a minimum of -5.1 ± 1.4 kJ mol^{-1} for the intermediate composition $x = 1.0$ (Fig. 10b and Table 8), which is about half of the minimum ΔH_{mix} value when related to x (Fig. 7b). A fit of the ΔH_{mix} data *versus* y was produced by calculating ΔH_{mix} values from the quadratic fit of ΔH_{ds} *versus* y using eqn (7). The minimum value of ΔH_{mix} calculated is -3.9 kJ mol^{-1}. This is approximately half of the calculated minimum of ΔH_{mix} *versus* x. The nearly linear behavior of ΔH_{ds} and suppressed parabolic behavior of ΔH_{mix} with respect to y indicates that the system can be considered a mixture of ordered pyrochlore and disordered weberite-type domains (except the two endmembers) with little interfacial or nanoscale interactions between them. This trend agrees well with the accumulation of weberite-type atomic arrangements in the form of coherent nanodomains across the entire compositional range determined from structural analysis (Fig. 8). In contrast, when ΔH_{ds} is plotted against the long-range defect fluorite $Fm\bar{3}m$ phase fraction, f, the behavior deviates dramatically from a linear trend and shows a sigmoidal evolution (Fig. 10a). Since there is no evidence for a sharp change in enthalpy near the critical composition of the pyrochlore-to-defect fluorite transition ($x \approx 1.2$), it can be concluded that the long-range structure is not the driving force for the thermodynamics of the system.

While the weberite-type structure is more ordered than defect fluorite, it is still partially disordered and may have less order than in reported clusters of rare earth stabilized fluorite phases, which may explain the less negative interaction parameter. Alternatively, the substitution of rare earth cations in other defect fluorite phases, such as yttria-stabilized zirconia (YSZ), involves the creation and ordering of charge-balanced defects (trivalent cations and oxygen anion vacancies), while in the system studied here the total number of vacancies and charge on the cation sublattices are fixed by the $A_2B_2O_7$ stoichiometry, with only their ordering and distribution varying. Thus, electrostatic factors may be less important, consistent with less exothermic mixing. In addition, the weberite-type structure is not constrained to have the same composition as the matrix, with a given bulk composition, x, being the only overall compositional constraint. To further analyze the thermodynamic data in the complex $Ho_2Ti_{2-x}Zr_xO_7$ system, quantitative atomistic models are needed that describe the heats, entropies, and free energies of mixing. How much configurational entropy remains in these partially ordered structures remains a major question. High temperature *in situ* diffraction and differential scanning calorimetry studies can be done in the future to find the temperature dependence of the equilibrium degree of disorder and provide a more realistic thermodynamic model, as has been done for other pyrochlore compounds.[93] However, since at present we have data only for one series of quenched materials, we cannot say anything definitive about the equilibrium degree of

ordering and resulting configurational entropy. Further local structure and calorimetry studies of more fluorite-related systems would provide insights about the relation between local structure and thermodynamics.

5. Conclusions

We have investigated in detail how disordering proceeds across the $Ho_2Ti_{2-x}Zr_xO_7$ solid solution series from the long-range structure to the local atomic configuration. Combined neutron and X-ray total scattering, with high sensitivity to both cation and anion sublattices, reveal a complex order–disorder transition across different length scales induced by chemical substitution of Ti by Zr. Disordering proceeds locally through gradual accumulation of a weberite-type ($C222_1$) phase (linearly with increasing Zr-content x), which is in stark contrast to the step-like transition over the long-range from the pyrochlore structure ($Fd\bar{3}m$) to the defect fluorite structure ($Fm\bar{3}m$) at $x \approx 1.2$. Comparison of the local and average phase behavior and the polyhedral layering patterns in pyrochlore and weberite indicates that weberite-type building blocks are created at a distance from each other when Zr replaces Ti through the introduction of oxygen Frenkel defects. Weberite-type building blocks increase in number with increasing Zr-content until a critical concentration, which is followed by the appearance of defect fluorite in the long-range structure (when approximately 50% of Ti is replaced by Zr). The weberite-type building blocks (essentially weberite-type nanodomains) form within the pyrochlore matrix such that the configurational average of all potential orientations yields the long-range defect fluorite structure beyond the critical accumulation point. Analysis of the diffuse scattering supports this claim and further suggests that intermediate-range interactions play a critical role in the progression of the order–disorder transition. The thermodynamic data obtained from high temperature oxide melt solution calorimetry indicate that the energetics across the solid solution series closely follow the short-range phase behavior (phase fraction of weberite domains) rather than the transformation from pyrochlore to defect fluorite. The large extent of short-range ordering implies that one should not apply simple models, like regular solution, to these systems because of the inherent complexity of the entropy of mixing term. This complexity must be considered when analyzing other similar systems and when seeking new materials with desirable properties.

Author contributions

D. D., E. O., and M. L. conceived and designed the study. A. F. provided samples for the study. D. D., E. O., J. N., M. E., I. G., and M. L. performed the neutron total scattering experiments and analyzed the data. D. D., I. G., D. S., and M. L. performed the X-ray total scattering experiments and analyzed the data. T. S., K. L., and A. N. performed the high temperature melt solution calorimetry and analyzed the data. D. D. and G. B. performed diffuse scattering analysis on all total scattering data. D. D., E. O., T. S., A. N., G. B., R. E., and M. L. interpreted the data.

D. D. drafted the manuscript with input from and critical review by all authors.

References

1 M. A. Subramanian, G. Aravamudan and G. V. Subba Rao, *Prog. Solid State Chem.*, 1983, **15**, 55–143.

2 R. C. Ewing, W. J. Weber and J. Lian, *J. Appl. Phys.*, 2004, **95**, 5949–5971.

3 B. C. Chakoumakos, *J. Solid State Chem.*, 1984, **53**, 120–129.

4 B. J. Kennedy, *Phys. B*, 1997, **241–243**, 303–310.

5 H. Nyman, S. Andersson, B. G. Hyde and M. O'Keeffe, *J. Solid State Chem.*, 1978, **26**, 123–131.

6 P. J. Wilde and C. R. A. Catlow, *Solid State Ionics*, 1998, **112**, 173–183.

7 K. E. Sickafus, L. Minervini, R. W. Grimes, J. A. Valdez, M. Ishimaru, F. Li, K. J. McClellan and T. Hartmann, *Science*, 2000, **289**, 748–751.

8 L. Minervini, R. W. Grimes and K. E. Sickafus, *J. Am. Ceram. Soc.*, 2000, **83**, 1873–1878.

9 B. J. Wuensch, K. W. Eberman, C. Heremans, E. M. Ku, P. Onnerud, E. M. E. Yeo, S. M. Haile, J. K. Stalick and J. D. Jorgensen, *Solid State Ionics*, 2000, **129**, 111–133.

10 F. X. Zhang, M. Lang, Z. Liu and R. C. Ewing, *Phys. Rev. Lett.*, 2010, **105**, 015503.

11 F. X. Zhang, J. W. Wang, J. Lian, M. K. Lang, U. Becker and R. C. Ewing, *Phys. Rev. Lett.*, 2008, **100**, 045503.

12 W. R. Panero, L. Stixrude and R. C. Ewing, *Phys. Rev. B: Condens. Matter Mater. Phys.*, 2004, **70**, 054110.

13 M. T. Weller, R. W. Hughes, J. Rooke, C. S. Knee and J. Reading, *Dalton Trans.*, 2004, 3032–3041, DOI: 10.1039/b401787k.

14 Y. Shimakawa and Y. Kubo, *Mater. Sci. Eng., B*, 1999, **63**, 44–48.

15 C. Heremans, B. J. Wuensch, J. K. Stalick and E. Prince, *J. Solid State Chem.*, 1995, **117**, 108–121.

16 X. Cao, *J. Mater. Sci. Technol.*, 2007, **23**, 15–35.

17 P. K. Moon and H. L. Tuller, *Sens. Actuators, B*, 1990, **1**, 199–202.

18 S. X. Wang, B. D. Begg, L. M. Wang, R. C. Ewing, W. J. Weber and K. V. G. Kutty, *J. Mater. Res.*, 1999, **14**, 4470–4473.

19 K. E. Sickafus, R. W. Grimes, J. A. Valdez, A. Cleave, M. Tang, M. Ishimaru, S. M. Corish, C. R. Stanek and B. P. Uberuaga, *Nat. Mater.*, 2007, **6**, 217.

20 S. Finkeldei, M. C. Stennett, P. M. Kowalski, Y. Ji, E. de Visser-Týnová, N. C. Hyatt, D. Bosbach and F. Brandt, *J. Mater. Chem. A*, 2020, **8**, 2387–2403.

21 M. Lang, M. Toulemonde, J. Zhang, F. Zhang, C. L. Tracy, J. Lian, Z. Wang, W. J. Weber, D. Severin, M. Bender, C. Trautmann and R. C. Ewing, *Nucl. Instrum. Methods Phys. Res., Sect. B*, 2014, **336**, 102–115.

22 D. M. Strachan, R. D. Scheele, E. C. Buck, J. P. Icenhower, A. E. Kozelisky, R. L. Sell, R. J. Elovich and W. C. Buchmiller, *J. Nucl. Mater.*, 2005, **345**, 109–135.

23 R. D. Shannon, *Acta Crystallogr., Sect. A: Cryst. Phys., Diffr., Theor. Gen. Crystallogr.*, 1976, **32**, 751–767.

24 B. J. Wuensch and K. W. Eberman, *JOM*, 2000, **52**, 19–21.

25 S. T. Norberg, S. Hull, S. G. Eriksson, I. Ahmed, F. Kinyanjui and J. J. Biendicho, *Chem. Mater.*, 2012, **24**, 4294–4300.

26 M. Lang, F. Zhang, J. Zhang, J. Wang, J. Lian, W. J. Weber, B. Schuster, C. Trautmann, R. Neumann and R. C. Ewing, *Nucl. Instrum. Methods Phys. Res., Sect. B*, 2010, **268**, 2951–2959.

27 M. Lang, J. Lian, J. Zhang, F. Zhang, W. J. Weber, C. Trautmann and R. C. Ewing, *Phys. Rev. B: Condens. Matter Mater. Phys.*, 2009, **79**, 224105.

28 J. Lian, K. B. Helean, B. J. Kennedy, L. M. Wang, A. Navrotsky and R. C. Ewing, *J. Phys. Chem. B*, 2006, **110**, 2343–2350.

29 Y. Li, P. M. Kowalski, G. Beridze, A. R. Birnie, S. Finkeldei and D. Bosbach, *Scr. Mater.*, 2015, **107**, 18–21.

30 C. Jiang, C. R. Stanek, K. E. Sickafus and B. P. Uberuaga, *Phys. Rev. B: Condens. Matter Mater. Phys.*, 2009, **79**, 104203.

31 Y. Liu, R. L. Withers and L. Norén, *J. Solid State Chem.*, 2004, **177**, 4404–4412.

32 E. M. Ku, E. M. E. Yeo and B. J. Wuensch, *MRS Proc.*, 1998, **547**, 327.

33 N. Kim and C. P. Grey, *J. Solid State Chem.*, 2003, **175**, 110–115.

34 M. de los Reyes, K. R. Whittle, Z. Zhang, S. E. Ashbrook, M. R. Mitchell, L.-Y. Jang and G. R. Lumpkin, *RSC Adv.*, 2013, **3**, 5090–5099.

35 Z. Zhang, S. C. Middleburgh, M. de los Reyes, G. R. Lumpkin, B. J. Kennedy, P. E. R. Blanchard, E. Reynolds and L.-Y. Jang, *J. Phys. Chem. C*, 2013, **117**, 26740–26749.

36 M. Shafique, B. J. Kennedy, Y. Iqbal and R. Ubic, *J. Alloys Compd.*, 2016, **671**, 226–233.

37 M. Glerup, O. F. Nielsen and F. W. Poulsen, *J. Solid State Chem.*, 2001, **160**, 25–32.

38 P. E. R. Blanchard, R. Clements, B. J. Kennedy, C. D. Ling, E. Reynolds, M. Avdeev, A. P. J. Stampfl, Z. Zhang and L.-Y. Jang, *Inorg. Chem.*, 2012, **51**, 13237–13244.

39 P. E. R. Blanchard, S. Liu, B. J. Kennedy, C. D. Ling, M. Avdeev, J. B. Aitken, B. C. C. Cowie and A. Tadich, *J. Phys. Chem. C*, 2013, **117**, 2266–2273.

40 S. V. Ushakov, A. Navrotsky, J. A. Tangeman and K. B. Helean, *J. Am. Ceram. Soc.*, 2007, **90**, 1171–1176.

41 M. P. Saradhi, S. V. Ushakov and A. Navrotsky, *RSC Adv.*, 2012, **2**, 3328–3334.

42 J. Shamblin, M. Feygenson, J. Neuefeind, C. L. Tracy, F. Zhang, S. Finkeldei, D. Bosbach, H. Zhou, R. C. Ewing and M. Lang, *Nat. Mater.*, 2016, **15**, 507.

43 G. King, C. M. Thompson, J. E. Greedan and A. Llobet, *J. Phys. Chem. A*, 2013, **1**, 10487–10494.

44 J. Shamblin, C. L. Tracy, R. I. Palomares, E. C. O'Quinn, R. C. Ewing, J. Neuefeind, M. Feygenson, J. Behrens, C. Trautmann and M. Lang, *Acta Mater.*, 2018, **144**, 60–67.

45 I. M. Gussev, E. C. O'Quinn, G. Baldinozzi, J. Neuefeind, R. C. Ewing, F. Zhang and M. Lang, *Acta Mater.*, 2020, **196**, 704–709.

46 E. C. O'Quinn, K. E. Sickafus, R. C. Ewing, G. Baldinozzi, J. C. Neuefeind, M. G. Tucker, A. F. Fuentes, D. Drey and M. K. Lang, *Sci. Adv.*, 2020, **6**, eabc2758.

47 M. Wakeshima, H. Nishimine and Y. Hinatsu, *J. Phys.: Condens. Matter*, 2004, **16**, 4103–4120.

48 J. M. Solomon, J. Shamblin, M. Lang, A. Navrotsky and M. Asta, *Sci. Rep.*, 2016, **6**, 38772.

49 E. C. O'Quinn, J. Shamblin, B. Perlov, R. C. Ewing, J. Neuefeind, M. Feygenson, I. Gussev and M. Lang, *J. Am. Chem. Soc.*, 2017, **139**, 10395–10402.

50 S. Finkeldei, P. Kegler, P. M. Kowalski, C. Schreinemachers, F. Brandt, A. A. Bukaemskiy, V. L. Vinograd, G. Beridze, A. Shelyug, A. Navrotsky and D. Bosbach, *Acta Mater.*, 2017, **125**, 166–176.

51 E. C. O'Quinn, J. L. Bishop, R. Sherrod, J. Neuefeind, S. M. Montemayor, A. F. Fuentes and M. Lang, *J. Mater. Sci.*, 2018, **53**, 13400–13410.

52 T. A. Lee and A. Navrotsky, *J. Mater. Res.*, 2004, **19**, 1855–1861.

53 T. A. Lee, A. Navrotsky and I. Molodetsky, *J. Mater. Res.*, 2003, **18**, 908–918.

54 A. Navrotsky, *J. Mater. Chem.*, 2010, **20**, 10577–10587.

55 A. Navrotsky, P. Simoncic, H. Yokokawa, W. Chen and T. Lee, *Faraday Discuss.*, 2007, **134**, 171–180.

56 P. Simoncic and A. Navrotsky, *J. Am. Ceram. Soc.*, 2007, **90**, 2143–2150.

57 P. Simoncic and A. Navrotsky, *J. Mater. Res.*, 2007, **22**, 876–885.

58 X. Guo, S. Szenknect, A. Mesbah, N. Clavier, C. Poinssot, D. Wu, H. Xu, N. Dacheux, R. C. Ewing and A. Navrotsky, *Chem. Mater.*, 2016, **28**, 7117–7124.

59 C.-K. Chung, J. Shamblin, E. C. O'Quinn, A. Shelyug, I. Gussev, M. Lang and A. Navrotsky, *Acta Mater.*, 2018, **145**, 227–234.

60 C.-K. Chung, E. C. O'Quinn, J. C. Neuefeind, A. F. Fuentes, H. Xu, M. Lang and A. Navrotsky, *Acta Mater.*, 2019, **181**, 309–317.

61 C.-K. Chung, M. Lang, H. Xu and A. Navrotsky, *Acta Mater.*, 2018, **155**, 386–392.

62 T. Subramani and A. Navrotsky, *Inorg. Chem.*, 2019, **58**, 16126–16133.

63 J. Neuefeind, M. Feygenson, J. Carruth, R. Hoffmann and K. K. Chipley, *Nucl. Instrum. Methods Phys. Res., Sect. B*, 2012, **287**, 68–75.

64 A. K. Soper and E. R. Barney, *J. Appl. Crystallogr.*, 2012, **45**, 1314.

65 S. G. Eric Dooryhee, M. Rehak and X. Shi, *Preliminary Design Report for the X-ray Powder Diffraction (XPD) Beamline at NSLS-II, NSLS-II*, Brookhaven National Lab, 2010.

66 X. Shi, S. Ghose and E. Dooryhee, *J. Synchrotron Radiat.*, 2013, **20**, 234–242.

67 P. Juhas, T. Davis, C. L. Farrow and S. J. L. Billinge, *J. Appl. Crystallogr.*, 2013, **46**, 560–566.

68 R. B. Von Dreele and B. H. Toby, *J. Appl. Crystallogr.*, 2013, **46**, 544–549.

69 V. F. Sears, *Neutron News*, 1992, **3**, 26–37.

70 *X-ray Form Factor, Attenuation and Scattering Tables (version 2.1)*, http://physics.nist.gov/ffast, accessed March 2020.

71 C. L. Farrow, P. Juhas, J. W. Liu, D. Bryndin, E. S. Božin, J. Bloch, T. Proffen and S. J. L. Billinge, *J. Phys.: Condens. Matter*, 2007, **19**, 335219.

72 G. Paglia, E. S. Božin, D. Vengust, D. Mihailovic and S. J. L. Billinge, *Chem. Mater.*, 2006, **18**, 100–106.

73 V. Petkov, S. J. L. Billinge, P. Larson, S. D. Mahanti, T. Vogt, K. K. Rangan and M. G. Kanatzidis, *Phys. Rev. B: Condens. Matter Mater. Phys.*, 2002, **65**, 092105.

74 R. B. Neder, F. Frey and H. Schulz, *Acta Crystallogr., Sect. A: Found. Crystallogr.*, 1990, **46**, 792–798.

75 A. Navrotsky and O. J. Kleppa, *Inorg. Chem.*, 1967, **6**, 2119–2121.

76 A. Navrotsky, *J. Am. Ceram. Soc.*, 2014, **97**, 3349–3359.

77 A. Navrotsky, *Phys. Chem. Miner.*, 1977, **2**, 89–104.

78 A. Navrotsky, *Phys. Chem. Miner.*, 1997, **24**, 222–241.

79 A. Navrotsky, *Am. Mineral.*, 2015, **100**, 674–680.

80 S. Hayun and A. Navrotsky, *J. Solid State Chem.*, 2012, **187**, 70–74.

81 V. L. Vegard, *J. Mater. Sci.*, 1921, **1**, 79–90.

82 K. R. Whittle, L. M. D. Cranswick, S. A. T. Redfern, I. P. Swainson and G. R. Lumpkin, *J. Solid State Chem.*, 2009, **182**, 442–450.

83 T. Egami and S. J. L. Billinge, *Underneath the Bragg Peaks: Structural Analysis of Complex Materials*, Pergamon, Oxford, 2012.

84 L. Cai and J. C. Nino, *Acta Crystallogr., Sect. B: Struct. Sci.*, 2009, **65**, 269–290.

85 J. H. Hildebrand, *J. Am. Chem. Soc.*, 1929, **51**, 66–80.

86 J. Ganguly, *EMU Notes in Mineralogy*, 2001, vol. 3, pp. 37–69.

87 R. A. Swalin, *Am. J. Phys.*, 1962, **30**, 778.

88 D. K. Smith and W. Newkirk, *Acta Crystallogr.*, 1965, **18**, 983–991.

89 J. D. McCullough and K. N. Trueblood, *Acta Crystallogr.*, 1959, **12**, 507–511.

90 G. Pilania, B. Puchala and B. Uberuaga, *npj Comput. Mater.*, 2019, **5**, 7.

91 C. L. Tracy, M. Lang, F. Zhang, C. Trautmann and R. C. Ewing, *Phys. Rev. B*, 2015, **92**, 174101.

92 P. K. Davies and A. Navrotsky, *J. Solid State Chem.*, 1983, **46**, 1–22.

93 P. S. Maram, S. V. Ushakov, R. J. K. Weber, C. J. Benmore and A. Navrotsky, *Sci. Rep.*, 2018, **8**, 1–11.